Experimental assessment of the performance of a bridge pier subjected to flood-induced foundation scour

Accepted manuscript doi:
10.1680/jgeot.20.P.230

Submitted: 03 July 2020

Published online in 'accepted manuscript' format: 10 May 2021

Manuscript title: Experimental assessment of the performance of a bridge pier subjected to flood-induced foundation scour

Authors: Andrea Ciancimino*, Liam Jones†, Lampros Sakellariadis†, Ioannis Anastasopoulos† and Sebastiano Foti*

Affiliations: *Department of Structural, Geotechnical and Building Engineering, Politecnico di Torino, Italy and †Chair of Geotechnical Engineering, ETH Zurich, Switzerland

Corresponding author: Andrea Ciancimino, Department of Structural, Geotechnical and Building Engineering, Politecnico di Torino, Italy.

E-mail: andrea.ciancimino@polito.it

Accepted manuscript doi:
10.1680/jgeot.20.P.230

Abstract

Scouring around piers is recognized as one of the main causes of bridge failure. Local scour refers to the localized erosion of soil at piers and abutments caused by flow-induced vortices around their base. This paper studies experimentally the response of a bridge pier, supported on a cylindrical embedded foundation, subjected to flood-induced scour. A hybrid 2-step methodology is developed to study the *hydraulic* and the *mechanical* part of the problem. In the first step, the *hydraulic* problem of local scour around a pier is experimentally modelled in 1***g*** using a recently developed Miniaturized Tidal Generator. The experimentally generated scour hole is then 3D-scanned to produce a 3D-printed mould. The latter is used in the second step to reproduce the scour hole in an *N**g*** model, subsequently tested in a drum centrifuge to study the *mechanical* part of the problem under proper stress scaling. Foundation performance *prior* and *after* local scour is studied through vertical, lateral monotonic, and slow-cyclic pushover tests. The effects of general (uniform) scour are also investigated by removing a soil layer of constant thickness. Local scour is shown to have a minor effect on vertical bearing capacity. In stark contrast, the lateral performance is significantly affected, with the foundation moment capacity M_{ult} being reduced by up to 38%. The effect of general scour is even more pronounced, leading to 48% reduction of M_{ult}. The rate of cyclic settlement accumulation is also much more severely affected by general compared to local scour. Overall, the effects of *local* scour on foundation performance differ substantially to those of *general scour*, questioning the common simplification of ignoring the geometry of the scour hole, making no distinction between local and general scour.

Keywords: Footings/foundations; erosion; centrifuge modelling; soil/structure interaction; bearing capacity; earthquakes

Accepted manuscript doi:
10.1680/jgeot.20.P.230

INTRODUCTION

The localized loss of support caused by scouring around bridge piers is one of the main causes of bridge failure (Ballio et al., 1998; Melville & Coleman, 2000). Wardhana & Hadipriono (2003) documented 503 bridge failures that occurred in the United States between 1989 and 2000. Almost half (48%) of these failures were due to flooding and scour, resulting in significant damage (requiring costly repairs), or even collapse and loss of human lives.

Scour typically takes place around bridge piers (or abutments) founded in water (e.g., riverbed), being the result of the erosive action of flowing water. It encompasses three components (Melville & Coleman, 2000): (i) long-term degradation of the riverbed; (ii) contraction scour; and (iii) local scour. Long-term streambed elevation changes are the result of aggradation and degradation phenomena, which occur naturally in riverbeds, but can also be the result of changes in the hydraulic parameters of the channel. Contraction scour is due to the reduction of the river cross-section as a result of the construction of the bridge. Both of the first two components lead to a global erosion of the riverbed and are thus usually identified as *general* (or *global*) *scour*. The third component, *local scour*, refers to the very localized erosion around bridge piers, caused by the flow-induced vortices around their base.

Such vortices remove soil material from the base of the piers, leading to the development of a scour hole. As the scour depth increases, the vortices strength decreases until equilibrium is re-established (Melville & Coleman, 2000; Richardson & Davis, 2001). Two different local scour regimes can be identified (Melville & Coleman, 2000): (a) clear-water, when no sediments are transported by the water flow (or at most, when the soil is transported in suspension); and (b) livebed scour, when sediments delivered by the river interact with the scour process. While in the first case, the scour depth increases slowly until equilibrium is reached, in the second case the interaction with the transported sediments leads to cyclic refilling of the scour hole.

Scour around piers affects foundation response, and may therefore affect the overall performance of the bridge. Its effect is related to soil erosion (loss of material and change of geometry), but also changes of the stress state of the underlying remaining soil (e.g., Lin et al., 2010; Lin et al., 2014; Qi et al., 2016; Liang et al., 2017). Zhang et al. (2019) conducted a series of 1***g*** physical model tests to study the response of two foundation systems (caisson and composite caisson-piled foundation) to long-term cyclic lateral loading, with and without local scour. The removal of soil around the foundation was shown to lead to a significant reduction of its lateral bearing capacity, and a non-negligible increase of accumulated settlement due to cyclic loading.

During the last decade or so, vibration-based monitoring techniques have been proposed to study the evolution of the dynamic response of bridges due to scour (e.g., Briaud et al., 2011; Foti & Sabia, 2011; Prendergast & Gavin, 2014; Bao & Liu, 2017). The results have proven that the erosive process affects the seismic performance of the soil-structure system, leading to a significant reduction of foundation stiffness.

Local scour phenomena have been extensively studied from a *hydraulic* point of view, leading to empirical predictive equations of the maximum scour depth (e.g., Breusers & Raudkivi, 1991; Melville & Coleman, 2000; Sumer & Fredsøe, 2002; Sheppard & Renna, 2005; Arneson et al., 2012). In contrast, only a few experimental studies have focused on the effects of scouring on the *mechanical* response of the foundation (e.g., Prendergast et al., 2013; Elsaid & Seracino, 2014; Qi et al., 2016; Zhang et al., 2019). The two aspects of the problem (*hydraulics* and *mechanics*) are analysed separately, and the assessment of the performance of scoured piers is performed without considering a well-defined water flow scenario. The hydraulics predictive equations are used to estimate the maximum scour depth,

and the local scour hole is modelled crudely: either by removing a constant thickness soil layer (no distinction between general and local scour) or by considering an idealized scour hole geometry (a cone sloping at the critical state friction angle). The real geometry and the asymmetry of the scour hole is neglected (e.g., Elsaid & Seracino, 2014; Qi et al., 2016; Zhang et al., 2019). However, recent studies (Foti & Sabia, 2011; Liang et al., 2019; Kariyawasam et al., 2020) suggest that the scour hole geometry may have a significant effect on the mechanical response of the soil-structure system.

This paper presents an experimental study on the influence of scouring on the mechanical response of a single-column bridge pier founded on a cylindrical embedded foundation. A 2-step methodology is developed to study the *hydraulic* and the *mechanical* part of the problem. In the first step, a novel experimental apparatus is employed to conduct *hydraulic* 1$\boldsymbol{g}$ physical model tests, to simulate the development of the local scour hole due to a well-defined hydraulic scenario. In the second step, the results of *hydraulic* 1$\boldsymbol{g}$ tests are used to reproduce the actual geometry of the scour hole in *N*$\boldsymbol{g}$ physical models tested in a geotechnical centrifuge, to study the *mechanical* response of the scoured foundation. The influence of local scour on foundation performance is investigated through monotonic vertical and lateral pushover tests, and slow-cyclic lateral push tests. Although the paper focuses on local scour, the effects of general scour (i.e., erosion of a constant thickness soil layer) are also investigated to reveal and quantify the differences between these two distinct processes.

PROBLEM DEFINITION AND EXPERIMENTAL METHODOLOGY

An idealized single degree of freedom (SDOF) system is considered, representing a prototype bridge pier of height $h = 6.8$ m, supported on a cylindrical foundation of diameter $D = 2$ m and embedment depth $d = 2$ m, founded on dense sand (Fig. 1). Since the focus is on foundation performance, a rigid pier is considered. The bridge deck is represented by a concentrated mass m_1, adjusted to achieve a factor of safety against vertical loading $FS_v \approx 8$ before scouring (including the pier and foundation masses, m_2 and m_3, respectively). The selected FS_v, which corresponds to a moderately loaded structure, is calculated based on the vertical bearing capacity of the foundation, experimentally measured through a vertical push test conducted in the geotechnical centrifuge.

A novel hybrid approach is developed to study the mechanical behaviour of the foundation subjected to flood-induced scour due to a well-defined hydraulic scenario. A 2-step methodology is employed, decoupling the *hydraulic* (i.e. the scour process around the bridge pier) and the *mechanical* part of the problem, as summarized in Fig. 2. The first step simulates the *hydraulic* process through small-scale (1:50) 1$\boldsymbol{g}$ physical model tests under clear-water conditions (Fig. 2a). The experiments are conducted employing a Miniaturised Tidal Generator (MTG; Jones & Anastasopoulos, 2020). The results of these tests can be used to define the scour depth and, most importantly, the morphology of the scour hole, acquired through a 3D scanner.

After digital processing, the inverse of the scour hole surface is 3D printed to produce a mould of the scour hole (Fig. 2b). The 3D-printed mould is used to reproduce the measured geometry of the scour hole (from Step 1) in a centrifuge model (Fig. 2c), which is subsequently tested (Step 2) in the ETHZ drum centrifuge (Springman et al., 2001). The second step addresses the mechanical part of the problem, using 1:*N* scaled models tested at *N*$\boldsymbol{g}$, thus achieving correct scaling of the in-situ stresses. The performance of the bridge pier is studied through vertical push tests, monotonic lateral pushover tests and lateral slow-cyclic tests. Table 1 summarizes the relevant scaling laws for both 1$\boldsymbol{g}$ and *N*$\boldsymbol{g}$ physical model tests.

The underlying assumptions of the hybrid two-step methodology are: (1) 1***g*** experiments are appropriate to reproduce the *hydraulic* scouring process; and (2) the scouring process does not strongly influence the void ratio of the remaining (unscoured) soil (i.e., the void ratio at the end of the scouring process is still uniform in the model). The first hypothesis is widely adopted in hydraulic experiments, where small and medium scale tests are conducted to study the scour phenomenon and the results are analyzed according to dimensionless quantities (e.g., Melville & Raudkivi, 1996; Coleman, 2005; Moreno et al., 2016). Furthermore, the effectiveness of the *hydraulic* 1***g*** tests is verified by comparing the results with predictions given by widely used empirical models. The second hypothesis is considered reasonable, especially in clear-water conditions, where no sediments are transported by the river or the material is transported in suspension (Melville & Coleman, 2000). No interaction is expected between the transported material and the scour process, and the soil is progressively eroded until the equilibrium scour depth is reached. The only part of the model where this hypothesis may not be verified is the depositional mound which forms at the exit slope from the scour hole (Arneson et al., 2012). This is, however, a relatively small zone downstream of the bridge, where the scour hole is shallower, which is not expected to significantly influence the *mechanical* response of the structure.

The direct (fully coupled) physical modelling of both the *hydraulic* and the *mechanical* part of the problem in a geotechnical centrifuge would be the best option to simulate the entire process as realistically as possible, provided that proper scaling of the water flow can be achieved. However, this would require a MTG mounted in the geotechnical centrifuge, which is not currently feasible. The developed decoupled approach represents a good balance between the reliability of the results and feasibility of physical model tests.

1***g*** PHYSICAL MODELLING OF LOCAL SCOUR

A series of 1:50 scale 1***g*** experiments is conducted to study the development of the local scour hole around the idealized bridge pier. The foundation-structure model consists of a cylindrical aluminium foundation of 40 mm diameter and height ($D = 2$ m in prototype scale), attached to a cylindrical aluminium pier of 12 mm diameter ($D_p = 0.6$ m in prototype scale). The experiments were conducted employing the ETHZ MTG (Fig. 2a), which can produce arbitrary waves or pseudo-steady flows through a system of pressure-controlled water tanks (Jones & Anastasopoulos, 2020). In the present study, the tanks are configured to act as a pumping system, which draws water from one side of the apparatus and discharges it at the opposite end. The removable model box is placed in the main channel and subjected to a long pseudo-steady flow. High precision ultrasonic sensors are used to measure the water level in the tank(s) $h_{t,i}$, and the flow depth y_0 directly upstream of the pier (Fig. 3). By knowing the geometry of the two tanks and $h_{t,i}$, it is possible to compute the total volume of water V_w discharged in time $\bar{t}$. Consequently, the mean flow rate $\bar{Q}$ is computed as $V_w/\bar{t}$. The mean velocity $\bar{v}$ of the water flow is thus obtained as the ratio of $\bar{Q}$ to the flow area, given by the mean flow depth $\bar{y}_0$ times the model width.

The time evolution of the scour hole around the bridge pier is monitored trough still images taken by a Digital Single-Lens Reflex (DSLR) camera at evenly spaced time intervals of 10 s. A series of circles with a spacing of 1 mm was engraved on the lateral surface of the foundation to allow effective tracking of the scour depth. The shape of the scour hole is acquired through a high precision 3D scan (3D Systems Corporation, Sense 2) with a spatial resolution of 0.9 mm and a depth resolution of 1 mm (i.e., about 5 cm in prototype scale). Scans are taken at different instants and at the end of the scour process, when the equilibrium scour depth is reached.

Accepted manuscript doi:
10.1680/jgeot.20.P.230

Model preparation and test programme

The 1$\boldsymbol{g}$ local scour tests, as well as the subsequent centrifuge tests, were conducted using fine Perth silica sand, with index properties summarized in Table 2. The values reported are based on previous studies (Nater, 2005; Buchheister, 2009), except the maximum void ratio $e_{\max}$, for which a value of 0.87 was measured according to Method A proposed in ASTM D425-16. The models are prepared outside the MTG, using a removable container of 50 cm length and 26 cm width (Fig. 2a), encompassing permeable lateral boundaries to allow for equilibration of pore water pressures inside the channel. The dry sand is pluviated in the container using a sand-raining system (Morales, 2015) to obtain the desired void ratio e of 0.56±0.02.

As summarized in Table 3, three *hydraulic* 1$\boldsymbol{g}$ tests were conducted with mean water flow velocities: $\bar{v}$ = 109.1 mm/s, 98.6 mm/s, and 62.9 mm/s. The water flow velocity $\bar{v}$ is normalized to the critical velocity U_c , obtained from Neill's (1967) equation, as a function of the mean grain size of the sand, d_{50}. The critical velocity defines the beginning of sediment motion and, therefore, of live-bed scour conditions (Melville & Coleman, 2000). A value of $\bar{v}/U_c < 1$ suggested that scouring will develop under clear-water regime, as required for the tests conducted herein. The three water flow velocities were thus selected to cover a wide range of $\bar{v}/U_c$, being sure of not exceeding the critical velocity.

At this point, a crucial issue requires clarification. When dealing with the mechanics of soil-structure interaction (as is the case for the centrifuge tests of Step 2), assuming that the soil behaves as a continuum, the d_{50} of the sand does not need to be scaled (i.e., the same sand can be used to model the prototype) – provided that some basic requirements are met. In contrast, when modelling a scour process, the actual particle size distribution influences the development of the scour hole. The value of U_c at prototype scale cannot be obtained by applying the usual 1$\boldsymbol{g}$ scaling laws to the corresponding value computed at model scale. Hence, the $\bar{v}/U_c$ ratio has to be computed at model scale, adopting the actual d_{50} of the sand. This ratio is the key parameter defining the scour regime, and consequently the expected scour depth. Therefore, the results of the scour tests are considered representative of prototype problems with $\bar{v}/U_c$ ratios consistent with the ones obtained at model scale (Table 3).

Test results

The key results of the conducted scour tests are presented and discussed in prototype scale. Figure 4 depicts the evolution of scouring in terms of average scour depth d_s (i.e., the scour depth measured along the longitudinal direction of the bridge) as a function of normalized time t^*:

$$t^* = \frac{t \cdot \bar{v}}{D_p} \tag{1}$$

where: D_p is the pier diameter. The plot also shows the maximum scour depth $d_{s,\max}$, observed at the end of each test along the upstream side. The difference between $d_{s,\max}$ and d_s increases with time, due to the developing asymmetry of the scour hole. After an initial phase in which a rapid increase is observed, the scour depth keeps increasing with a reduced pace, until asymptotically reaching its maximum value, in accord with the expected trends for local scour in clear-water conditions (Arneson et al., 2012). A maximum scour depth of about 1.1 m is observed for Test S1 ($\bar{v}/U_c$= 0.7). The decrease of the $\bar{v}/U_c$ ratio leads to a decrease of the maximum scour depth, reaching a value of 0.5 m for test S3 ($\bar{v}/U_c$= 0.4). The maximum scour depths are of the same order of magnitude of the water depth, as expected for wide piers in relatively shallow flows (Arneson et al., 2012).

Accepted manuscript doi:
10.1680/jgeot.20.P.230

In theory, a longer time would be required to ensure that the equilibrium scour depth is reached for a specific *hydraulic* scenario (Melville & Chiew, 1999). However, in the conducted tests no significant changes were observed after $t^* \approx 6000$ to 8000, which was defined as the reference final condition. In principle, some minor changes could affect the scour depth if the water flow was kept constant for a much longer time. This is not anyway within the scope of this study, which aims at quantifying the mechanical consequences of scouring for a defined hydraulic scenario of a specified water flow lasting for a specified time.

Figure 5 presents the progression of the scour hole with dimensionless time t^* for test S1 ($\bar{v}/U_c = 0.7$), in terms of contour plots of bed elevation (Fig. 5a) and transverse (with respect to the bridge axis) cross-sections at the foundation centreline (Fig. 5b). Initially, for $t^* = 1090$, the scour hole starts developing along the foundation flanks and the eroded soil is deposited downstream. The scour hole progressively extends around the foundation, and the initial gentle slope becomes steeper ($t^* = 2730$). For $t^* > 4380$, the maximum scour depth $d_{s,max} \approx 1.1$ m is reached, upstream. However, the scour hole is not yet fully developed, especially along the sides of the foundation, where it reaches a depth of 0.7 m.

The final configuration ($t^* = 8730$), corresponding to the equilibrium scour depth, is characterized by a scour hole with a maximum upstream slope of about 30°, which is equal to the constant volume friction angle, φ'_{cv}, of Perth sand (Buchheister, 2009). Downstream, the depositional zone is reduced, and a gentle slope can be observed, connecting the scour depth of about 0.5 m to the original ground surface. Along the longitudinal direction (with respect to the bridge axis, i.e., perpendicular to the flow direction), the scour hole is reasonably symmetric, with a scour depth slightly lower than the maximum. The final shape of the scour hole is totally consistent with widely accepted guidelines (e.g., Melville & Coleman, 2000; Arneson et al., 2012).

The final scour hole (t^* = 8730) obtained from Test S1 is used as a reference for the centrifuge model tests of Step 2 (mechanical problem), aiming to investigate a scenario where the effects of scouring on the behaviour of the foundation are maximized. The 3D-scanned geometry is initially regularized to obtain a symmetric shape in the transverse direction, which converges to the initial flat surface at the side boundaries (Fig. 5c). Then, moulds of the scour hole were 3D printed (using a Dremel 3D40 printer with a resolution of 0.3 mm), appropriately scaled to match the scale of the centrifuge model tests of Step 2.

Verification against existing empirical models

In this section, the experimental results are validated against the maximum scour depth predicted by two widely adopted empirical models for local scour around complex piers (i.e., piers supported by a larger diameter caisson or a caisson-pile foundation) under clear-water conditions. The comparisons are presented and discussed in prototype scale. It should be mentioned that, in the predictive models, the scour depth is always expressed as a function of dimensionless groups. Therefore, it is straightforward to apply the $1\boldsymbol{g}$ scaling laws of Table 1 to convert the scour depth from model to prototype scale.

The first empirical method is the one proposed in the Hydraulic Engineering Circular Nr.18, HEC-18, of the Federal Highway Administration (Arneson et al., 2012). The method relies on the equation initially proposed by Richardson & Davis (2001), and subsequently updated by Arneson et al. (2012). It is based on the hypothesis of superposition, according to which the maximum equilibrium scour depth can be computed separately for the pier ($d_{s,p}$) and the foundation ($d_{s,f}$), and the total maximum scour depth of the complex pier is obtained by the sum of the two components. The method accounts for the shielding effect offered by

the foundation overhang distance in front of the pier. A correction for wide piers in shallow flows (as suggested by Johnson & Torrico, 1994) is also applied.

The second empirical method is the one proposed by Coleman (2005), which is based on the concept of an equivalent pier diameter D_e, as the diameter of a single column that would produce the same scour depth with the complex system. Different equations are proposed to compute D_e, according to the distance of the bed elevation to the top of the foundation before scouring (equal to 0 in our case). The scour depth is then computed through the Melville & Coleman (2000) equation, applying the correction suggested by Parola et al. (1996) to account for the foundation shielding effect.

The two empirical methods are applied to estimate the (maximum) equilibrium scour depth for the conditions of the three laboratory tests, as summarized in Table 4. Both methods provide almost the same predictions of $d_{s,\max}$, namely 1.2 m, 1.1 m, and 0.7 m for Test S1, S2, and S3, respectively. The empirical estimates of $d_{s,\max}$ are in good agreement with the experimental results (1.1 m, 0.95 m, and 0.5 m, respectively), slightly overestimating the scour depth by 0.1 m to 0.2 m. Bearing in mind that the empirical predictive methods are supposed to be conservative, the comparison is quite acceptable. Moreover, the shape of the scour hole (as previously discussed) is consistent with results reported in the literature (e.g., Melville & Coleman, 2000; Arneson et al., 2012). It may, therefore, be concluded that the 1$\boldsymbol{g}$ tests are adequate to model the scour process and the results can be used to study the mechanics part of the problem in the geotechnical centrifuge.

CENTRIFUGE MODELLING: EXPERIMENTAL SETUP

In the second step, a series of centrifuge model tests were performed in the ETHZ geotechnical drum centrifuge (Broadbent & Sons Ltd). The centrifuge has an outer diameter of 2.2 m and a channel width of 0.7 m and is capable of 440$\boldsymbol{g}$ centrifugal acceleration carrying a payload of 2 t (Springman et al., 2001). The vertical push tests were performed at 100$\boldsymbol{g}$, while the horizontal ones at 50$\boldsymbol{g}$.

Model preparation

The models are prepared outside the centrifuge in strongboxes and subsequently installed in the drum channel, following the procedure suggested by Laue et al. (2002). Two models with the same instrumentation (models A and B) are placed symmetrically in the centrifuge and tested simultaneously to maintain channel balance. Sand pluviation is conducted following the same procedure as for the scour tests. Once the foundation level is reached, the model structure is placed on the soil along with the 3D printed mould of the scour hole (Fig. 2b). The sand is then pluviated through the mesh of the mould around the foundation. The regularized scour hole geometry obtained in equilibrium conditions during Test S1 (Fig. 5c) is adopted as a reference scenario. Once the target ground level is reached, the soil is saturated and then partially de-saturated (using porous stones, placed at the bottom of the strongboxes), leading to an unsaturated specimen with an apparent cohesion. This process allows the strongbox to be rotated by 90° to be mounted on the drum channel, keeping the model stable until the centrifuge starts spinning. At the end of the de-saturation process, the mould is removed reproducing the shape of the scour hole (Fig. 2c). Subsequently, the strongboxes are installed in the channel and the sensors and actuators are connected. The centrifuge is spun to the desired $\boldsymbol{g}$-level and the tests conducted.

During the spinning up phase, the models are again saturated using two water tanks connected via check valves to the strongboxes. The valves are initially closed, and the water tanks are filled up to the desired level of the water table defined by a couple of standpipes, providing water from outside to the channel. The inlet valves are then opened to saturate the

model boxes. As the hydraulic head difference between the standpipes and the boxes is reduced, the saturation process slows down, avoiding undesired changes of the scour hole morphology (as also confirmed by the onboard cameras). The choice of using water as saturation fluid implies the well-known discrepancy between the scaling laws for diffusion and dynamic time (see Table 1). However, the present study focuses on the behaviour of the foundation under drained conditions, and therefore this discrepancy is not of relevance. The whole process is monitored by Pore-water Pressure Transducers (PPTs). The latter showed a hydrostatic distribution of the water pressure, ensuring a high degree of saturation. Once the models are saturated, the loading is applied to the structures. At the end of the test, the water is drained through the outlet valves to keep the models stable when the centrifuge stops spinning.

Foundation-structure modelling

In the case of the vertical push tests, carried out at 100$\boldsymbol{g}$, only the footing is necessary: an aluminium cylinder of 20 mm diameter and height. For the horizontal pushover tests, conducted at 50$\boldsymbol{g}$, the physical model (Fig. 6) also includes the pier, which corresponds to the idealized SDOF prototype system (Fig. 1). The foundation is an aluminium cylinder of 40 mm diameter and height, while the pier of 110 mm height is made of brass to ensure adequate stiffness and strength. A small aluminium plate was added to serve as a target for the laser transducers used to measure the horizontal displacements. The steel mass representing the deck is defined based on the desired vertical safety factor of the foundation, as previously discussed.

It is worth mentioning that due to the height of the SDOF system compared to the radius of the drum centrifuge, when the corresponding masses are converted from model to prototype scale, the radial error (Madabhushi, 2014) is not negligible. To that end, the actual radial distance of the mass is used to determine the mass scaling factor *N*, rather than the reference radius (2/3 of the model depth of interest). Concerning particle size effects, the ratio of the foundation diameter to d_{50} is equal to 87 and 174 at 100$\boldsymbol{g}$ and 50$\boldsymbol{g}$, respectively. Ovesen (1979) suggested a minimum ratio of 35 for shallow circular footings, while Remaud (1999) reported a ratio of 60 to study the lateral response of piles (see Garnier et al., 2007 for further details). Therefore, the obtained ratios are considered sufficiently large to neglect particle size effects.

Vertical push tests

The vertical push tests are conducted in cylindrical strongboxes of 400 mm diameter and 200 mm height. The boxes are filled with sand up to 140 mm, ensuring a distance between the foundation base and the bottom boundary of 6*D*, while the sidewalls are far away from the foundation (>9*D*), thus minimising undesired boundary effects. The experimental setup is presented in Fig. 7a. The tests are conducted under displacement-controlled loading, using a screw jack actuator installed on the tool platform. The actuator is equipped with a load cell and is initially disconnected from the footing (Fig. 7b). After spinning, the foundation is pushed with a constant velocity of 0.02 mm/s to a maximum displacement of 20 mm to obtain the vertical load-settlement ($V-w$) response. The normalized velocity $vD/c_v = 8{\cdot}10^{-4} < 10^{-2}$ is considered sufficient to ensure drained conditions according to Randolph & Hope (2004), where c_v = 500 mm^2/s (Qi et al., 2016) is the consolidation coefficient of fine silica sand.

Monotonic and cyclic lateral pushover tests

The lateral pushover tests are also displacement-controlled, employing electric screw-jack actuators (Concens, 35) rigidly attached to the semi-circular strongboxes of 320 mm height and 1050 mm length (Fig. 8a). The actuators are connected to the models through sliding hinges, with pins free to move in the vertical direction (Fig. 8b). This connection is essential to apply the desired horizontal displacement while allowing the structure to freely settle (or uplift) and rotate. The distance between the foundation and the bottom boundary is larger than 3*D*, while the distances of the foundation to the lateral sidewalls are larger than 4*D* and 12*D*, in the transverse and longitudinal direction, respectively, to minimise undesired boundary effects. The actuators are connected outside the drum centrifuge, and then the strongboxes are installed in the channel. During this phase, an external support is used to hold in position the pier, rigidly connected to the foundation. After installation, the support is removed, and the steel mass is connected to the pier. An electromagnetic system holds in-place the mass during the initial spin-up phase (Fig. 8b). When a centrifugal acceleration of 10$\boldsymbol{g}$ is reached, the system is released.

For each strongbox, a high-resolution load cell of 2kN capacity (MTS, Type 8523) is installed on the actuator to measure the horizontal force, H, applied to the structure. Three laser sensors (Micro-Epsilon, optoNCDT 1402) are used to measure the in-plane displacements of the structure: L_1 and L_2 measure horizontal displacements and L_3 vertical displacements (Fig. 8). As shown in Fig. 9, the rotation, θ, of the structure can be computed as:

$$\theta = \frac{u_{L_1} - u_{L_2}}{h_L} \tag{2}$$

where: u_{L_1} and u_{L_2} are the displacements measured by the horizontal laser sensors, while h_L is the distance between them. The settlement w of the structure (using the centre of the foundation as a reference) can be calculated as follows:

$$w = w_{L_3} + \left(\frac{h_{tot}}{\cos\theta} - h_{tot} + \left(u_{L_1} - h_{act} \cdot \tan\theta\right) \cdot \tan\theta\right) \tag{3}$$

where: w_{L_3} is the vertical displacement measured by laser sensor L_3, and h_{act} is the distance between the actuator (and also laser L_1) and the bottom of the footing. The overturning moment can be computed as:

$$M = H \cdot h_{act} \tag{4}$$

The model structures, considering scoured and unscoured conditions, are subjected to monotonic and slow-cyclic pushover loading. The monotonic tests are performed with a constant velocity of 0.5 mm/s up to a maximum displacement of 8 mm, which is adequate to measure the entire moment–rotation ($M - \theta$) response, all the way up to toppling. The slow-cyclic tests are performed according to a protocol that consists of 10 load cycles for 8 different increasing amplitudes. Two PPTs are embedded in the soil below the foundation (at 0.5*D* and 1*D*) to detect a potential undesired pore-water pressure build-up (Fig. 8a). The PPT measurements were found to be negligible, confirming the fully drained hypothesis of the tests.

In the following sections, the results are presented in prototype scale, according to the scaling laws of Table 1. The data were acquired with a sampling frequency of 100 Hz. A smoothing procedure was applied to the raw data through a 3rd order Savitzky-Golay filter using a built-in Matlab routine (MathWorks, 2020).

Accepted manuscript doi:
10.1680/jgeot.20.P.230

VERTICAL LOADING

The bearing capacity of the foundation subjected to purely vertical loading is investigated for unscoured and scoured conditions. As summarized in Table 5, four vertical push tests ($V1_{A,B}$ and $V2_{A,B}$) were conducted, checking also the repeatability of the experimental process. Fig. 10 presents the key results in terms of tangent vertical stiffness–settlement ($K_v - w$), and vertical load – settlement ($V - w$) response. The repeatability of the testing process is demonstrated by the comparison of the $K_v - w$ curves (Fig. 10a). Comparing each pair of tests for scoured and unscoured conditions, small discrepancies are observed but the results are consistent. For each case, the bearing capacity is estimated considering the average of the two tests.

Regarding the failure mode, a local shear mechanism was observed rather than a general one, as it should be expected for a relatively shallow footing on dense sand (Vesic, 1973, 1975). The $V - w$ curves (Fig. 10a) are slightly nonlinear up to a settlement $w = 0.15$ m. Then, the failure mechanism starts developing, and the response becomes highly nonlinear. Once the failure mechanism is fully developed, the curves exhibit an almost linear hardening response. The latter is partially due to the progressive increase of foundation embedment. Following the procedure suggested by Anastasopoulos et al. (2012), V_{ult} is defined as the load at the initiation of the hardening regime (i.e. the point at which the $K_v - w$ curves become horizontal), which corresponds to settlement w_{ult} (Fig. 10). Using this definition, V_{ult} = 8.93 MN in unscoured conditions. When considering scoured conditions, V_{ult} = 8.24 MN (i.e., a reduction of 7.8 %). This limited reduction is mainly due to the decrease of the effective overburden pressure in the soil below the foundation; the size of the local scour hole is not sufficient to intersect the failure surface.

The measured V_{ult} is used as a reference to determine the deck mass (Fig. 6) required to achieve a factor of safety under purely vertical loading FS_v of about 8, which corresponds to a moderately loaded bridge system. In the unscoured case, the achieved FS_v is 8.6, reducing to 7.95 with scouring.

LATERAL PUSHOVER LOADING

The lateral response is investigated through displacement-controlled monotonic pushover tests. The problem is symmetric in the longitudinal direction (y), and therefore a single test is adequate. In the transverse direction (x), given the asymmetry of the scour hole, two tests were necessary: one downstream and one upstream (Fig. 11). An additional model was realized by removing a uniform soil layer of 1 m thickness (i.e., the average scour depth due to local scour) to compare the effect of general (i.e., uniform) to local scour. The idealized SDOF structure can be considered representative for relatively long multi-span bridges loaded in the transverse direction. In the longitudinal direction, such a system can be representative provided that the deck is not monolithically connected to the piers (i.e., supported on bearings). Table 6 summarizes the conduced pushover tests (MH1-5), along with the measured moment capacity M_{ult} and the rotation angle at incipient overturning of the structure θ_{ult}.

Figure 12 reports the results of the tests in terms of the moment-rotation ($M - \theta$) response. The response of the scoured structure is compared to the reference case of unscoured conditions. The $M - \theta$ response exhibits an initial quasi-elastic branch, followed by strongly nonlinear response until full mobilization of the ultimate moment capacity M_{ult}, and a final descending branch (due to $P - \delta$, second-order, effects) until reaching the overturning rotation θ_{ult}. In all cases examined, the scouring leads to a substantial decrease of M_{ult}. In the case of local scour and loading in the transverse direction (Fig. 12a,b), M_{ult}

decreases from 19% to 27%, when loaded towards the downstream or the upstream side, respectively. The overturning rotation θ_{ult} is also reduced to 0.064 rad (downstream loading) and 0.067 rad (upstream loading), compared to 0.072 rad of the unscoured reference case. These differences, attributed to the larger volume of eroded soil along the upstream side (Fig. 11), are non-negligible, but also not excessive.

A much more significant reduction (38%) of M_{ult} is observed in the longitudinal direction (Fig. 12c), where a larger volume of soil is eroded from the sides of the foundation. The reduction of θ_{ult} is also more significant, decreasing from 0.072 rad (unscoured case) to 0.051 rad.

As expected, the maximum reduction of M_{ult} (48%) and θ_{ult} (0.048 rad) is observed in the case of general scour (Fig. 12d). In this case, the foundation embedment is simply reduced to $d = 1$ m (as opposed to 2 m before scouring). The results indicate that the simplified assumption of uniform scour can be excessively conservative, especially when considering the transverse direction of loading (which is usually critical). It may therefore be concluded that modelling the actual geometry of the scour hole, due to local scour processes, may have a significant effect on the conclusions and the decision regarding retrofit.

SLOW-CYCLIC LATERAL LOADING

According to Gajan & Kutter (2008) and Anastasopoulos et al. (2012), the results of slow-cyclic lateral pushover tests can be considered representative of the seismic performance of a foundation system. Three displacement-controlled slow-cyclic centrifuge model tests (CH1-3) are conducted to explore the effects of scouring on foundation performance. As summarized in Table 7, three cases were examined: unscoured (reference) condition; after local scour along the transverse direction of the bridge (which is usually critical); and after general scour.

As shown in Fig. 13, the displacement protocol consists of 8 packages of increasing displacement amplitude (2.5, 5, 7.5, 10, 15, 20, 30, and 40 cm in prototype scale), each one containing 10 load cycles. This allowed studying the slow-cyclic response of the foundation from small to large range of rotation. The load is applied at a sufficiently slow rate, maintaining a model frequency of 0.05 Hz (0.001 Hz in prototype scale), avoid possible dynamic effects that would further complicate the response.

Figure 14 compares the moment–rotation ($M-\theta$) and the settlement–rotation ($w-\theta$) response for the three cases examined. The monotonic response is also included to allows for comparison. Especially in Test CH3 (general scour), a non-negligible asymmetry in the $M-\theta$ response was observed during the last two packages (30 and 40 cm amplitude), which is attributed to excessive deformation. To allow for comparison, the last two packages are excluded from Test CH3. Consistently with the monotonic tests, the unscoured foundation exhibits the largest M_{ult} (Fig. 14a), followed by the one subjected to local scour (Fig. 14b), and general scour (Fig. 14c). Despite the previously discussed geometric asymmetry of the local scour hole, no significant asymmetries are observed in the $M-\theta$ loops.

Interestingly (but not surprisingly), the cyclic $M-\theta$ loops exhibit an overstrength compared to the monotonic backbone curve for all cases examined. The overstrength ratio r_M, can be defined as the increase in the cyclic moment capacity over the monotonic moment capacity M_{ult} (Kokkali et al., 2015). The r_M reaches 120% for the unscoured foundation, becoming even higher (135%) in the case of local scour, and going to an astonishing 210% under general scour conditions. As pointed out by Kokkali et al. (2015), the cyclic overstrength is mainly due to progressive soil densification, and to the increase of foundation embedment due to settlement accumulation. The increase of embedment is more substantial

for the scoured systems, leading to the larger r_M. In the case of general scour, settlement accumulation leads to a very pronounced increase of the embedment ratio from 0.5 to 1.

The observed overstrength can be better explained by looking into the settlement accumulation during cyclic loading (Fig. 15). The settlement w at the end of each cycle is plotted against the number of cycles in Fig. 15a. In contrast to local scour, which does not affect the rate of settlement accumulation considerably, general scour leads to a very pronounced increase. Fig. 15b depicts the evolution of cyclic settlement w_c (due to one cycle of loading) for the first 10-cycle package (of smallest amplitude), also in function of the number of cycles. In all cases examined, w_c decreases with the number of (constant amplitude) cycles. This reveals that (at least for small discplacement amplitudes), cyclic sand densification is the controlling parameter: sand densification leads to the observed decrease of settlement accumulated per cycle w_c.

The rate of settlement increases with the initiation of the following larger amplitude package. Fig. 15c plots the average settlement per cycle $\overline{w}_c$ for each 10-cycle package, as a function of cyclic rotation θ_c. For relatively small θ_c (< 0.01 rad), the accumulated settlement is mainly due to sand densification under the foundation, and hence the results are insensitive to scouring. The effect of scour becomes evident for larger θ_c (> 0.02 rad), where the moment capacity is fully mobilized and the rate of settlement is mainly controlled by soil plastification. General scour leads to a pronounced decrease of embedment, leading to a much shallower failure mechanism, leading to the observed drastic increase of $\overline{w}_c$. Local scour leads to a loss of side resistance, but not to such a pronounced decrease of embedment. As a result, the failure mechanism is not affected to the same extent, and hence its effect on $\overline{w}_c$ is less significant. For even larger θ_c, the dilative response of sand starts to compensate the plasticity-induced settlements, leading to progressive stabilization and even decrease of the rate of settlement, especially in the general scour case.

Effects of scouring on the rocking stiffness degradation and damping ratio curves

As shown in Gazetas et al. (2013), the degradation of secant rocking stiffness with rotation θ and the corresponding hysteretic damping ratio offer a convenient way to quantify nonlinear foundation response, and can also be used to assess dynamic performance based on equivalent-linear analyses. In this context, this section investigates the effects of scouring on the cyclic secant rocking stiffness $K_{r,c}$ and the hysteretic damping ratio $\xi_{r,h}$, as a function of θ. Their calculation is performed using the $M-\theta$ loops of the cyclic pushover tests, as shown in Fig. 16. The moment $\Delta M(\delta)$ caused by second-order $(P-\delta)$ effects is added to the external applied moment. During loading, $\Delta M(\delta)$ reduces the moment capacity leading to an additional *apparent* stiffness degradation. Conversely, as shown by Panagiotidou et al. (2012), during unloading $\Delta M(\delta)$ is opposed to the motion leading to an *apparent* overstrength. The latter also leads to enlargement of the $M-\theta$ loops, increasing hysteretic damping. Hence, $K_{r,c}$ is defined as the slope of the line connecting the edges of the $[M+\Delta M(\delta)]-\theta$ loops, and the $\xi_{r,c}$ as a function of the energy W_D dissipated within one such loop over the corresponding elastic energy W_S.

Fig. 17 plots the $K_{r,c}$ and $\xi_{r,h}$ curves obtained from the cyclic pushover tests. The average cyclic rocking stiffness of each load package (i.e., the average $K_{r,c}$ obtained for the 10 cycles of equal imposed displacement) is compared to the monotonic secant stiffness $K_{r,m}$ computed from the monotonic pushover tests, again correcting for $P-\delta$ effects. Due to measurement accuracy, the estimated $K_{r,m}$ for very small rotations is not considered reliable. Hence, the results are plotted for $\theta > 0.008$ rad, and curve-fitting is performed to roughly estimate the small-strain rocking stiffness (shown with dashed lines). The previously

Accepted manuscript doi:
10.1680/jgeot.20.P.230

discussed overstrength (Fig. 14) leads to a significant increase of $K_{r,c}$ in comparison to $K_{r,m}$. Nevertheless, the trends are consistent between cyclic and monotonic tests. General scour leads to a pronounced reduction of the secant rocking stiffness for the entire range of θ; the effect of local scour is moderate. Despite the geometric asymmetry of the scour hole, the direction of loading (upstream or downstream) does not significantly affect the $K_{r,m}$ curves. This is consistent with the shape of the $M-\theta$ loops, which are only slightly skewed (Fig. 14b). The hysteretic damping ratio $\xi_{r,h}$ increases with rotation θ, reaching a maximum of 0.4 to 0.5. Despite the difference in secant stiffness, the damping ratio is insensitive to the degree of scouring.

Fig. 18 offers direct visualization of the effect of the number of cycles on nonlinear rocking response. The cyclic secant rocking stiffness $K_{r,c}$, normalized to the estimated small-strain monotonic rocking stiffness $K_{r,m}(\theta = 0)$, is plotted for the 1st, 3rd and 10th cycle of each θ_c amplitude (from the corresponding load packages); the same is applied to the hysteretic damping ratio $\xi_{r,h}$. For all cases examined, the normalized secant rocking stiffness $K_{r,c} \,/\, K_{r,m}(\theta = 0)$ increases during the first two packages, tending to stabilize during the ensuing larger amplitude packages. This tendency is present in the unscoured case (Fig. 18a), but is more pronounced when the foundation is subjected to local (Fig. 18b) and general scouring (Fig. 18c), where sand densification is accompanied by an increase of embedment (due to the progressive accumulation of settlement). The increase of embedment, as previously discussed, leads to a significant overstrength when the cyclic response is compared to the monotonic one, which reflects in $K_{r,c}$ values at small rotations even higher than $K_{r,m}(\theta = 0)$. In stark contrast, $\xi_{r,h}$ is insensitive to the number of cycles. However, it should be pointed out that at very small rotations it is challenging to define very precisely the shape of the hysteresis loops due to the accuracy of the instrumentation. Therefore, minor differences between $\xi_{r,h}$ measured at different small amplitude cycles may not have been detected.

CONCLUSIONS

This paper reports on an experimental study on the response of a moderately loaded ($FS_v \approx 8$) bridge pier, supported on a cylindrical embedded foundation, subjected to flood-induced scour. A hybrid 2-step methodology was developed for this purpose. In the first step, the hydraulic problem of local scour around a pier is modelled in 1$\boldsymbol{g}$. The scour hole morphology is 3D-scanned and a mould is 3D-printed to reproduce the geometry in an $N\boldsymbol{g}$ model, subsequently tested in the ETHZ drum centrifuge to study its mechanical response. The methodology was applied to investigate the performance of the soil-structure system prior and after local scour through vertical, lateral monotonic, and lateral slow-cyclic pushover tests. An additional test series was conducted to study the effects of general scour, removing a layer of constant thickness equal to the maximum measured local scour depth. The key conclusions of the study are summarized as follows:

1) Local scour has a limited effect on the vertical response of the foundation. In stark contrast, the lateral response is significantly affected, with the foundation moment capacity M_{ult} being reduced by 19% to 38%, depending on the direction of loading. General scour has an even more pronounced effect, leading to 48% reduction of M_{ult}. It may therefore be concluded that accounting for the scour hole geometry is essential to address the effects of local scour. Assuming general scour conditions can be largely over-conservative.
2) For all the investigated configurations, the slow-cyclic pushover tests reveal a significant overstrength compared to the monotonic backbone curve and the corresponding M_{ult}.

These differences, quantified through the moment overstrength ratio r_M, are attributed to progressive sand densification, and to the increase of embedment due to settlement accumulation. While local scour leads to a small increase of r_M, the effect of general scour is pronounced. This is mainly attributed to the drastic increase of the embedment ratio from 0.5 to 1, due to the accumulation of settlement.

3) A pronounced increase of the settlement rate is observed due to general scour. The increase is mainly attributed to the significant loss of embedment that leads to a shallower failure mechanism and a substantial decrease of FS_v . This is not the case for local scour, which only leads to a small decrease of FS_v, thus not significantly affecting the failure mechanism and the rate of settlement accumulation.
4) In contrast to general scour, which leads to a pronounced reduction of the secant rocking stiffness $K_{r,m}$ for the entire range of θ, local scour has a moderate effect. Despite the observed asymmetry of the scour hole, the secant rocking stiffness is insensitive to the loading direction. The hysteretic damping ratio $\xi_{r,h}$ increases with rotation θ, but seems to be insensitive to scouring.

Overall, the effects of *local scour* on foundation response are significantly different from those of *general scour*. However, in practice the shape of the local scour hole is typically neglected, making no distinction between local and general scour. The evolution of the scour process is usually simulated by progressively removing soil layers of constant thickness (e.g., Alipour et al., 2012; Wang et al., 2014; Klinga & Alipour, 2015; Liang et al., 2017) – a simplification considered to be conservative. Considering static loading, the experimental results of this study confirm this hypothesis, indicating however, that such simplified assumption can be over-conservative, especially for the transverse direction of loading.

This is not necessarily the case for dynamic loading. Nonlinear soil–foundation response has been shown to be potentially beneficial for the seismic response of the superstructure (e.g., Gazetas et al., 2003; Pecker, 2003; Gajan et al., 2005; Gajan & Kutter, 2008; Anastasopoulos et al., 2010; Loli et al., 2014), something that can be of great relevance for the seismic retrofit of existing bridges. The reduction of foundation moment capacity M_{ult} leads to a reduction of inertia loading of the superstructure, at the cost of increased settlement. The simplifying assumption of general scour is therefore problematic, as the underestimation of M_{ult} (compared to local scour conditions) will lead to an *underestimation* of the inertia loading of the structure (*un-conservative*) and to an *overestimation* of permanent settlement (*over-conservative*). This can have major implications on the seismic retrofit of existing bridges, calling for realistic modelling of the geometry of the scour hole with due consideration of local scour processes.

Acknowledgements

The authors would like to express their gratitude to the head of the ETH geotechnical laboratory, R. Herzog, and the technicians M. Iten and E. Bleiker for their valuable support in performing the laboratory tests.

Notation

c_v	consolidation coefficient
C_u	uniformity coefficient
C_c	curvature coefficient
d	embedment depth
d_{50}	mean grain size
d_s	average scour depth

$d_{s,p}$, $d_{s,f}$	equilibrium scour depth due to the presence of the pier and the footing, respectively, according to the HEC-18 method
$d_{s,\max}$	maximum scour depth
D	diameter of the footing
D_e	equivalent single-column diameter
D_p	diameter of the pier
D_R	relative density
$e_{\min}$, $e_{\max}$, e	minimum, maximum and actual void ratio
FS_v	purely vertical safety factor
φ'_{cv}	constant volume friction angle
h	height of the structure, from the top of the footing to the mass center of the deck
h_{act}	distance between the actuator and the bottom of the footing
h_G	height of the mass center of the structure from the bottom of the footing
h_L	distance between the horizontal lasers
$h_{t,i}$	height of the column of water in the *i-th* pump-tank
H	horizontal force applied by the actuator
K_v	tangent vertical stiffness of the footing
$K_{r,c}$	secant cyclic rocking stiffness
$K_{r,m}$	secant monotonic rocking stiffness
$K_{r,m}(\theta = 0)$	small-strain rocking stiffness
m_1	mass of the deck
m_2	mass of the column
m_3	mass of the footing
M	rotational moment applied by the actuator
M_{ult}	ultimate moment capacity of the structure
$\Delta M(\delta)$	second-order moment
N	centrifugal acceleration
$P-\delta$	second-order effects
θ	rotation
θ_c	cyclic rotational amplitude
θ_{ult}	rotation angle at incipient overturning of the structure
$\bar{Q}$	mean flow rate
r_M	moment overstrength ratio defined as the increase in the cyclic moment capacity divided by the monotonic ultimate moment
t	time
t^*	normalized time equal to $t \cdot \bar{v}/D_c$
u_{L_1}, u_{L_2}	horizontal displacements measured by lasers L_1 and L_2, respectively
U_c	water flow critical velocity
$\bar{v}$	mean flow velocity
V	vertical load
V_{ult}	purely vertical bearing capacity of the footing
V_w	total volume of water discharged in time $\bar{t}$
w	settlement
w_c	settlement per cycle
$\bar{w}_c$	average settlement per cycle within one package of 10 cycles at constant loading amplitude

w_{L_3}	vertical displacement measured by laser L_3
w_{ult}	ultimate settlement associated to the vertical bearing capacity of the footing
$\xi_{r,h}$	hysteretic rocking damping ratio
y_0	flow depth
$\bar{y}_0$	mean flow depth

References

Alipour A, Shafei B, Shinozuka M (2012) Reliability-based calibration of load and resistance factors for design of RC bridges under multiple extreme events: Scour and earthquake *Journal of Bridge Engineering* 18:362-371

Anastasopoulos I, Gazetas G, Loli M, Apostolou M, Gerolymos N (2010) Soil failure can be used for seismic protection of structures *Bulletin of Earthquake Engineering* 8:309-326

Anastasopoulos I, Kourkoulis R, Gelagoti F, Papadopoulos E (2012) Rocking response of SDOF systems on shallow improved sand: An experimental study *Soil Dynamics and Earthquake Engineering* 40:15-33

Arneson L, Zevenbergen L, Lagasse P, Clopper P (2012) Evaluating scour at bridges: Hydraulic Engineering Circular No. 18. Washington DC, USA

ASTM International (2016) ASTM D4254-16, Minimum Index Density and Unit Weight of Soils and Calculation of Relative Density. ASTM International, West Conshohocken, PA

Ballio F, Bianchi A, Franzetti S, Mancini M Vulnerabilità idraulica di ponti fluviali (in Italian). In: *XXVI Convegno di Idraulica e Costruzioni Idrauliche*, 1998. pp 69-80

Bao T, Liu Z (2017) Vibration-based bridge scour detection: a review *Structural Control and Health Monitoring* 24:e1937

Breusers H, Raudkivi AJ (1991) Scouring. AA Balkema,

Briaud J-L et al. (2011) Realtime monitoring of bridge scour using remote monitoring technology. Texas Transportation Institute,

Buchheister JA (2009) Verflüssigungspotenzial von reinem und siltigem Sand unter multiaxialer Belastung (in German). vol Ph.D. Dissertation No. 18312. ETH Zurich, Zurich, Switzerland. doi:10.3929/ethz-a-006020660

Coleman SE (2005) Clearwater local scour at complex piers *Journal of Hydraulic Engineering* 131:330-334

Elsaid A, Seracino R (2014) Rapid assessment of foundation scour using the dynamic features of bridge superstructure *Construction and Building Materials* 50:42-49

Foti S, Sabia D (2011) Influence of foundation scour on the dynamic response of an existing bridge *Journal of Bridge Engineering* 16:295-304

Gajan S, Kutter BL (2008) Capacity, settlement, and energy dissipation of shallow footings subjected to rocking *Journal of Geotechnical and Geoenvironmental Engineering* 134:1129-1141

Gajan S, Kutter BL, Phalen JD, Hutchinson TC, Martin GR (2005) Centrifuge modeling of load-deformation behavior of rocking shallow foundations *Soil Dynamics and Earthquake Engineering* 25:773-783

Garnier J et al. (2007) Catalogue of scaling laws and similitude questions in geotechnical centrifuge modelling *International Journal of Physical Modelling in Geotechnics* 7:1

Gazetas G, Apostolou M, Anastasopoulos J Seismic uplifting of foundations on soft soil, with examples from Adapazari (Izmit 1999 earthquake). In: *BGA International Conference on Foundations: Innovations, observations, design and practice: Proceedings of the international conference organised by British Geotechnical Association and held in Dundee, Scotland on 2–5th September 2003*, 2003. Thomas Telford Publishing, pp 37-49

Johnson PA, Torrico EF (1994) Scour around wide piers in shallow water *Transportation Research Record*:66-70

Jones L, Anastasopoulos I Development of an Apparatus for the Simulation of Coastal Structures Subjected to Tsunami. In: *Proceedings of the 16th European Conference on Earthquake Engineering (16ECEE)*, 2018. European Association for Earthquake Engineering, p 11482

Jones L, Anastasopoulos I (2020) Miniaturised Tsunami Generator to model the Interaction of Tsunamis with Coastal infrastructure *International Journal of Physical Modelling in Geotechnics*:35 doi:10.1680/jphmg.19.00021

Kariyawasam KD, Middleton CR, Madabhushi G, Haigh SK, Talbot JP (2020) Assessment of bridge natural frequency as an indicator of scour using centrifuge modelling *Journal of Civil Structural Health Monitoring* 10:861-881

Klinga JV, Alipour A (2015) Assessment of structural integrity of bridges under extreme scour conditions *Engineering Structures* 82:55-71

Kokkali P, Anastasopoulos I, Abdoun T, Gazetas G Static and cyclic rocking on sand: centrifuge versus reduced-scale 1 g experiments. In: *Geotechnical Earthquake Engineering: Géotechnique Symposium in Print 2015*, 2015. ICE Publishing, pp 155-170

Laue J, Nater P, Springman SM Preparation of soil samples in drum centrifuges. In: *International Conference on Physical Modelling in Geotechnics/ICPGM'02, St. John's, New Foundland, Canada, 10-12 July 2002*, 2002. Balkema, pp 143-148

Liang F, Wang C, Yu X (2019) Widths, types, and configurations: Influences on scour behaviors of bridge foundations in non-cohesive soils *Marine Georesources & Geotechnology* 37:578-588

Liang F, Zhang H, Huang M (2017) Influence of flood-induced scour on dynamic impedances of pile groups considering the stress history of undrained soft clay *Soil Dynamics and Earthquake Engineering* 96:76-88

Lin C, Bennett C, Han J, Parsons RL (2010) Scour effects on the response of laterally loaded piles considering stress history of sand *Computers and Geotechnics* 37:1008-1014

Lin C, Han J, Bennett C, Parsons RL (2014) Behavior of laterally loaded piles under scour conditions considering the stress history of undrained soft clay *Journal of Geotechnical and Geoenvironmental Engineering* 140:06014005

Loli M, Knappett JA, Brown MJ, Anastasopoulos I, Gazetas G (2014) Centrifuge modeling of rocking-isolated inelastic RC bridge piers *Earthquake engineering & structural dynamics* 43:2341-2359

Madabhushi G (2014) Centrifuge modelling for civil engineers. CRC Press,

MathWorks (2020) MATLAB and Curve Fitting Toolbox, Release 2018a edn., Natick, Massachusetts, United States

Melville BW, Chiew Y-M (1999) Time scale for local scour at bridge piers *Journal of Hydraulic Engineering* 125:59-65

Melville BW, Coleman SE (2000) Bridge scour. Water Resources Publication, Highlands Ranch, CO, USA.

Melville BW, Raudkivi AJ (1996) Effects of foundation geometry on bridge pier scour *Journal of Hydraulic Engineering* 122:203-209

Morales P (2015) River dyke failure modeling under transient water conditions vol 247. vdf Hochschulverlag AG,

Moreno M, Maia R, Couto L (2016) Prediction of equilibrium local scour depth at complex bridge piers *Journal of Hydraulic Engineering* 142:04016045

Muir Wood D (2004) Geotechnical modelling. E & FN Spon,

Nater P (2005) Belastungs- und Verformungsverhalten von geschichteten Bodensystemen unter starren Kreisfundationen. (in German). ETH Zurich

Neill CR (1967) Mean-velocity criterion for scour of coarse uniform bed-material. Paper presented at the *12th IAHR Congress*, Fort Collins, CO,

Ovesen NK The scaling law relationship - Panel discussion. In: *Proc. 7th European Conference on Soil Mechanics and Foundation Engineering*, Brighton, 1979. pp 319-323

Panagiotidou AI, Gazetas G, Gerolymos N (2012) Pushover and seismic response of foundations on stiff clay: analysis with p-delta effects *Earthquake Spectra* 28:1589-1618

Parola A, Mahavadi S, Brown B, El Khoury A (1996) Effects of rectangular foundation geometry on local pier scour *Journal of Hydraulic Engineering* 122:35-40

Pecker A Aseismic foundation design process, lessons learned from two major projects: the Vasco de Gama and the Rion Antirion bridges. In: *ACI International Conference on Seismic Bridge Design and Retrofit. La Jolla, California*, 2003.

Prendergast LJ, Gavin K (2014) A review of bridge scour monitoring techniques *Journal of Rock Mechanics and Geotechnical Engineering* 6:138-149

Prendergast LJ, Hester D, Gavin K, O'sullivan J (2013) An investigation of the changes in the natural frequency of a pile affected by scour *Journal of Sound and Vibration* 332:6685-6702

Qi WG, Gao F, Randolph MF, Lehane BM (2016) Scour effects on p–y curves for shallowly embedded piles in sand *Géotechnique* 66:648-660

Randolph M, Hope S Effect of cone velocity on cone resistance and excess pore pressures. In: *Effect of cone velocity on cone resistance and excess pore pressures*, 2004. Yodogawa Kogisha Co. Ltd, pp 147-152

Remaud D (1999) Pieux sous charges latérales: étude expérimentale de l'effet de groupe. Université de Nantes

Richardson E, Davis S (2001) Evaluating scour at bridges: Hydraulic Engineering Circular No. 18. Washington DC, USA

Sheppard D, Renna R (2005) Bridge scour manual *Florida Department of Transportation, Florida*

Springman SM, Laue J, Boyle R, White J, Zweidler A (2001) The ETH Zurich geotechnical drum centrifuge *International Journal of Physical Modelling in Geotechnics* 1:59-70

Sumer BM, Fredsøe J (2002) The mechanics of scour in the marine environment. World Scientific,

Taeseri D, Laue J, Anastasopoulos I (2018) Non-linear rocking stiffness of embedded foundations in sand *Géotechnique*:1-16

Vesic AS (1973) Analysis of ultimate loads of shallow foundations *ASCE Journal of Soil Mechanics & Foundations Div* 99:45-73

Vesic AS (1975) Bearing capacity of shallow foundations. In: ed.s WaF (ed) Foundation engineering handbook. Van Nostran Reinhold, New York, pp 121-147

Wang Z, Dueñas-Osorio L, Padgett JE (2014) Influence of scour effects on the seismic response of reinforced concrete bridges *Engineering structures* 76:202-214

Wardhana K, Hadipriono FC (2003) Analysis of recent bridge failures in the United States *Journal of performance of constructed facilities* 17:144-150

Zhang C, Zhang X, Huang M, Tang H (2019) Responses of caisson-piles foundations to long-term cyclic lateral load and scouring *Soil Dynamics and Earthquake Engineering* 119:62-74

Table 1. Scaling laws for 1*g* and N*g* centrifuge model tests (Muir Wood, 2004; Madabhushi, 2014).

Quantity	Scaling factors (model/prototype)	
	1g	Ng (centrifuge)
Acceleration	1	N
Length	N^{-1}	N^{-1}
Mass	N^{-3}	N^{-3}
Force	N^{-3}	N^{-2}
Stress	N^{-1}	1
Strain	1	1
Time (diffusion)	N^{-1}*	N^{-2} *
Time (dynamic)	$N^{-0.5}$	N^{-1}

*assuming same fluid viscosity used in model and prototype

Table 2. Index properties of fine Perth silica sand (modified from Nater, 2005, and Buchheister, 2009).

Mean grain size, d_{50}: mm	Uniformity coefficient, C_u	Curvature coefficient, C_c	Specific gravity, G_S	Minimum void ratio, $e_{\min}$	Maximum void ratio, $e_{\max}$
0.23	1.79	1.26	2.65	0.50	0.87

Accepted manuscript doi:
10.1680/jgeot.20.P.230

Table 3. Main characteristics of the conducted 1g scour tests (all data in model scale).

Test	Mean flow rate, $\bar{Q}$: cm^3/s	Normalized flow velocity, $\bar{v}/U_c$	Mean flow depth, $\bar{y}_0$: [mm]	Void ratio, e	Relative density, D_R
S1	780	0.70	27.5	0.55	0.86
S2	702	0.63	27.4	0.55	0.86
S3	566	0.40	34.6	0.55	0.86

Table 4. Equilibrium scour depth predictions employing the HEC-18 (Arneson et al., 2012) and the Coleman (2005) method.

Test	HEC-18			Coleman (2005)		Experimental
	$d_{s,p}$: m	$d_{s,f}$: m	$d_{s,\max}$: m	D_e: m	$d_{s,\max}$: m	$d_{s,\max}$: m
S1	**0.30**	**0.91**	1.21	**0.84**	1.23	1.10
S2	**0.28**	**0.81**	1.10	**0.84**	1.12	0.95
S3	**0.24**	**0.49**	0.74	**0.84**	0.70	0.50

Table 5. Summary of the vertical push tests.

Test	Condition	Void ratio, e	Relative density, D_R	Settlement at failure, w_{ult}: m	Vertical bearing capacity, V_{ult}: MN		Vertical safety factor, FS_v
						Average	
$V1_A$	Unscoured	0.55	0.86	0.45	8.91	8.93	8.60
$V1_B$	Unscoured	0.54	0.89	0.47	8.96		
$V2_A$	Scoured	0.55	0.86	0.49	8.14	8.24	7.95
$V2_B$	Scoured	0.54	0.89	0.46	8.33		

Table 6. Summary of monotonic lateral pushover tests.

Test	Condition	Loading direction	Void ratio, e	Relative density, D_R	Moment capacity, M_{ult}: kNm	Percentage decrease	Overturning rotation, θ_{ult}: rad
MH1	Unscoured	–	0.56	0.84	554	–	0.072
MH2	Local Scour	Transverse Downstream	0.55	0.86	447	-19.3%	0.064
MH3	Local Scour	Transverse Upstream	0.56	0.84	406	-26.7%	0.067
MH4	Local Scour	Longitudinal	0.56	0.84	342	-38.3%	0.051
MH5	Gen. Scour	–	0.57	0.81	289	-47.8%	0.048

Table 7. Summary of the slow-cyclic horizontal tests.

Test	Condition	Loading direction	Void ratio, e	Relative density, D_R
CH1	Unscoured	–	0.55	0.86
CH2	Local Scour	Transverse	0.56	0.84
CH3	General Scour	–	0.56	0.84

Figure captions

Fig. 1. Problem definition: SDOF bridge pier subjected to flood-induced scour.

Fig. 2. Methodology: (a) development of the scour hole through the MTG and 3D scan of the surface; (b) 3D printed mould of the scour hole; and (c) reproduction of the geometry to prepare models suitable in the geotechnical drum centrifuge.

Fig. 3. 1g physical modelling of local scour: (a) MTG experimental set-up; (b) tank height $h_{t,i}(t)$ and flow depth $y_0(t)$ recorded by ultrasonic sensors (adapted from Jones & Anastasopoulos, 2018).

Fig. 4. Evolution of scour depth d_s with dimensionless time t^*, along with the maximum scour depth $d_{s,max}$ (measured along the upstream side) as a function of water flow scenario.

Fig. 5. Time evolution of the scour hole for test S1 ($\bar{v}/U_c = 0.7$): (a) scanned contour plots of bed elevation; (b) cross-sections at the foundation centreline; and (c) contour plot of the regularized surface used for the 3D printed mould.

Fig. 6. Model SDOF structures used for the lateral pushover centrifuge tests.

Fig. 7. Experimental setup for the vertical push tests: (a) schematic cross-section; and (b) photo taken just before a test.

Fig. 8. Experimental setup for the lateral pushover tests: (a) schematic cross-section (modified from Taeseri et al., 2018); and (b) photo taken just before one of the tests.

Fig. 9. Reference scheme adopted to study the rocking response of the pier.

Fig. 10. Vertical response of the footing before and after local scouring: (a) tangent vertical stiffness–settlement ($K_V - w$); and (b) load–settlement ($V - w$) response.

Fig. 11. Cross-sections of the scour hole: (a) transverse direction; and (b) longitudinal direction (referring to the bridge axis).

Fig. 12. Moment-rotation ($M - \theta$) response before and after the scouring for loading in: (a) transverse-downstream direction; (b) transverse-upstream direction; (c) longitudinal direction; and (d) general (uniform) scour assumption.

Fig. 13. Displacement protocol used for the slow-cyclic horizontal tests and the corresponding cyclic rotations.

Fig. 14. Slow-cyclic moment-rotation ($M - \theta$) and settlement-rotation ($w - \theta$) response for: (a) unscoured conditions; (b) local scour; and (c) general scour.

Fig. 15. Settlement accumulation during cyclic loading: (a) settlement w in function of number of cycles; (b) settlement per cycle w_c in function of number of cycles (1st package); and (c) mean settlement per cycle $\overline{w}_c$ in function of cyclic rotation θ_c.

Fig. 16. Calculation of secant rocking stiffness $K_{r,c}$ and hysteretic damping ratio $\xi_{r,c}$ on the basis of cyclic $M - \theta$ loops.

Fig. 17. Effects of scour on rocking stiffness degradation $K_{r,c}$ and and damping ratio $\xi_{r,h}$ as a function of rotation θ. The cyclic secant rotational stiffness is compared to secant monotonic stiffness (the dashed part of the curves is estimated by fitting).

Fig. 18. Influence of the number of cycles on normalized cyclic secant rocking stiffness $K_{r,c} \,/\, K_{r,m}(\theta = 0)$ and damping ratio $\xi_{r,h}$ in function of cyclic rotation θ_c for: (a) unscoured reference case; (b) local scour; and (c) general scour.

Accepted manuscript doi:
10.1680/jgeot.20.P.230

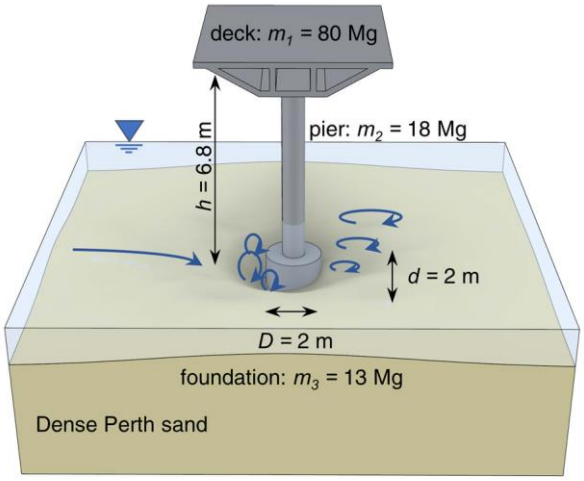

Fig.1

Accepted manuscript doi:
10.1680/jgeot.20.P.230

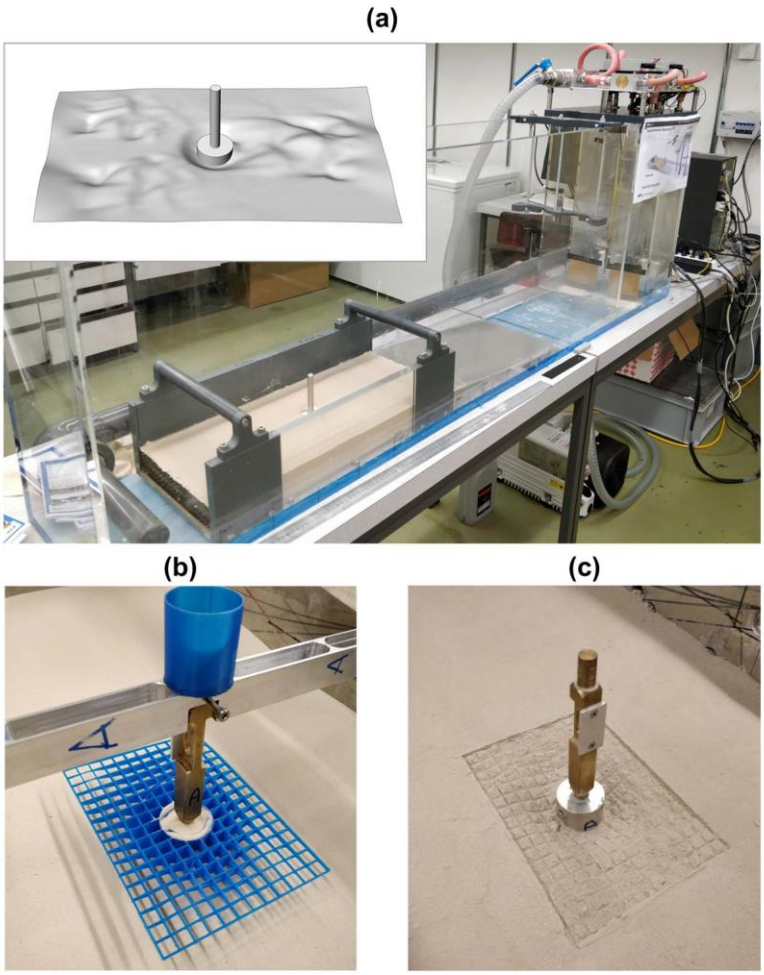

Fig.2

Accepted manuscript doi:
10.1680/jgeot.20.P.230

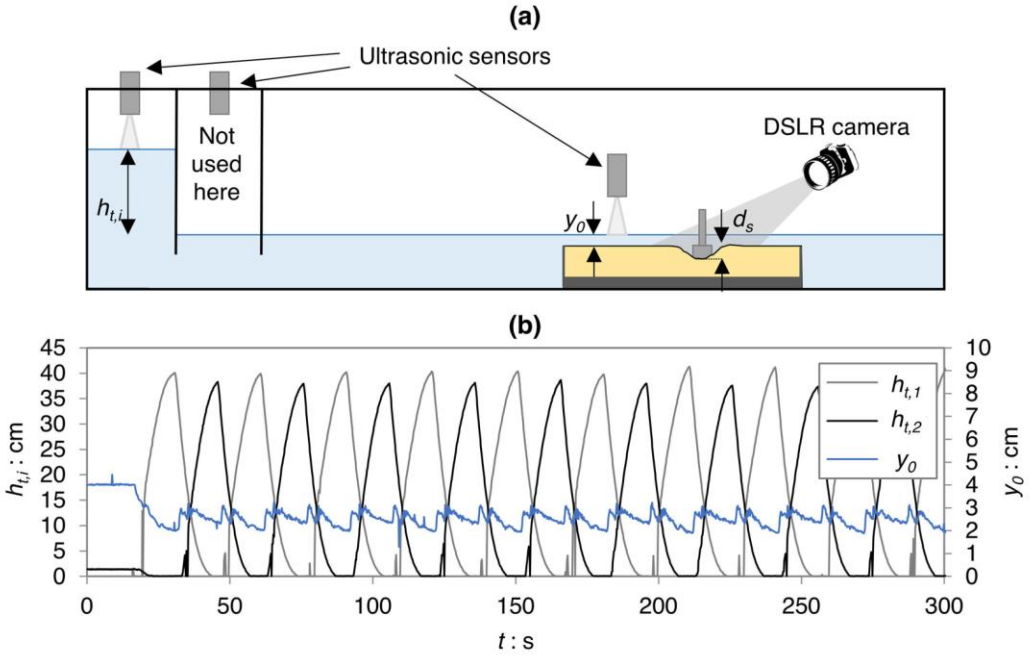

Fig.3

Accepted manuscript doi:
10.1680/jgeot.20.P.230

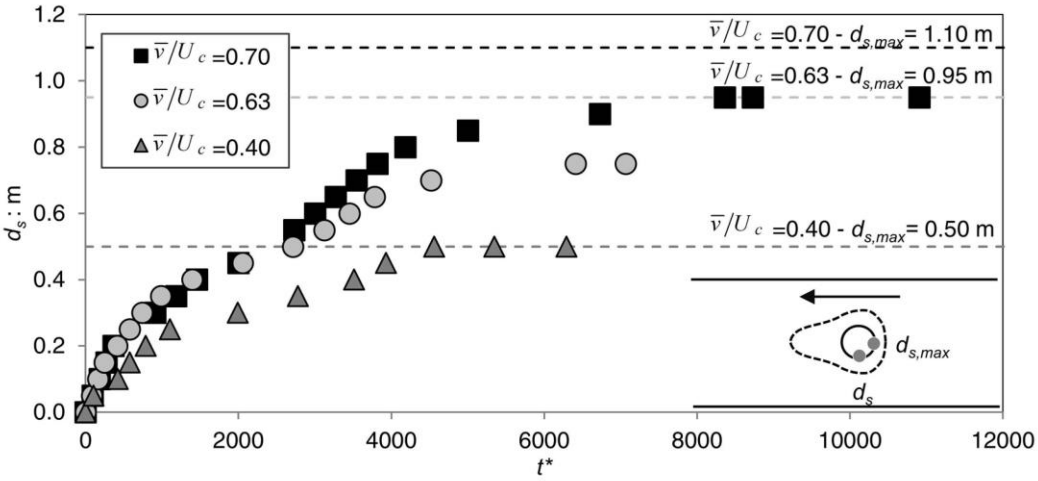

Fig.4

Accepted manuscript doi:
10.1680/jgeot.20.P.230

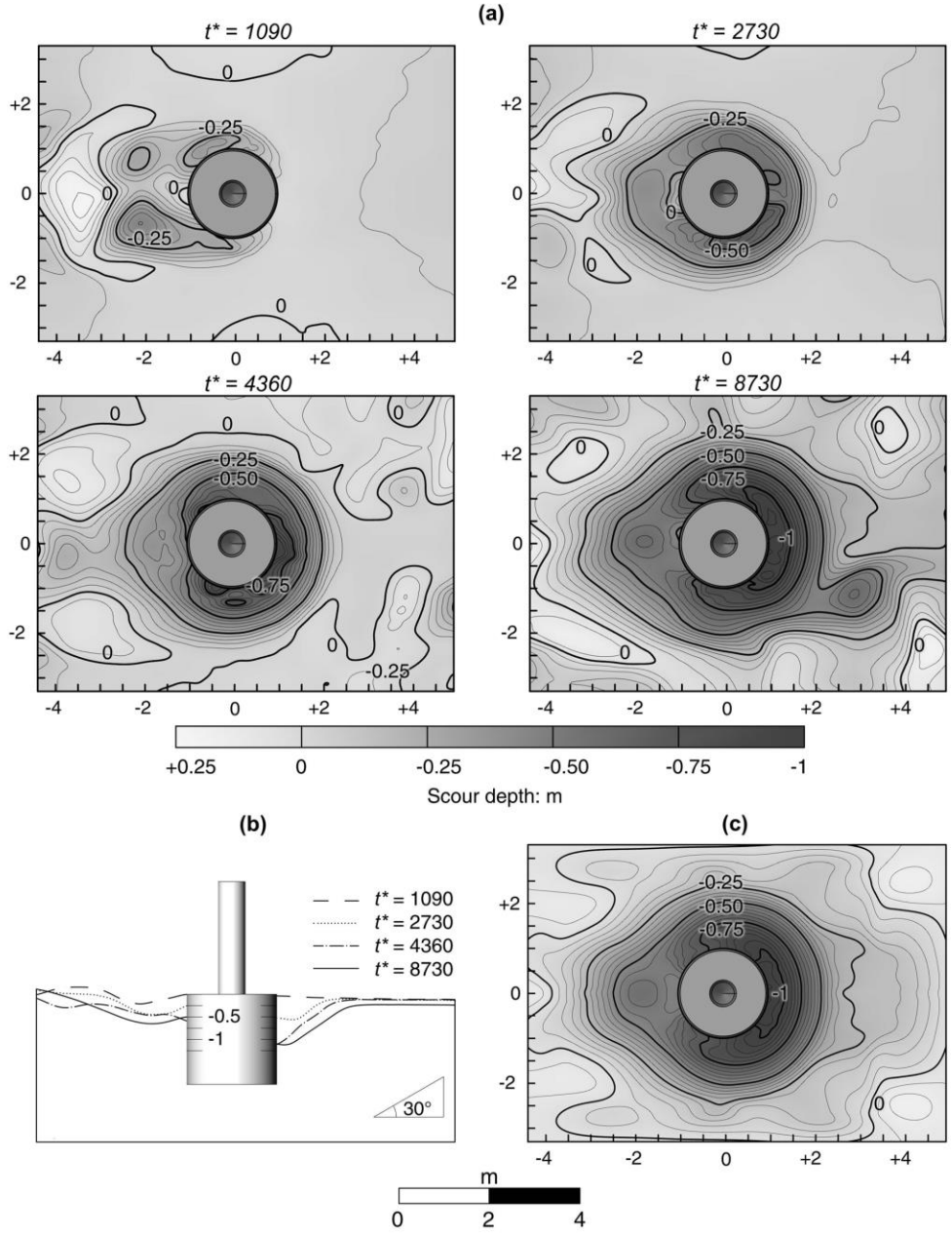

Fig.5

Accepted manuscript doi:
10.1680/jgeot.20.P.230

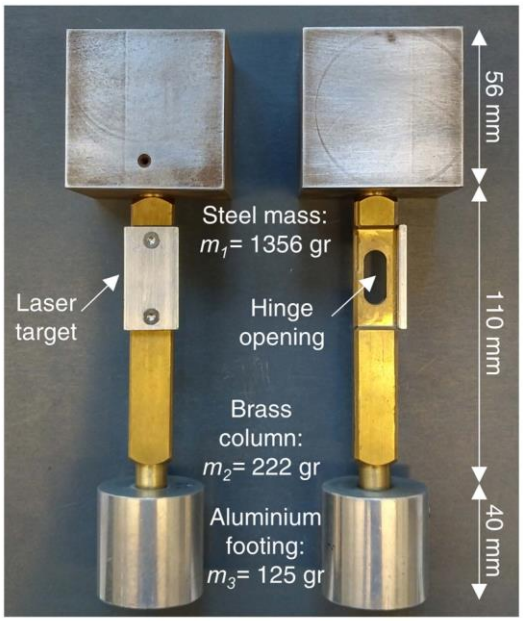

Fig.6

Accepted manuscript doi:
10.1680/jgeot.20.P.230

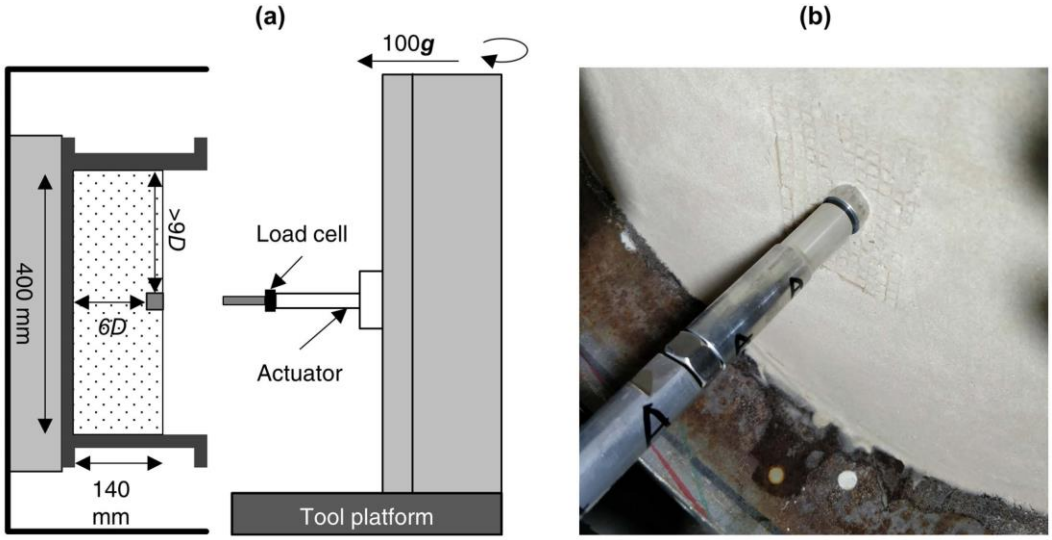

Fig.7

Accepted manuscript doi:
10.1680/jgeot.20.P.230

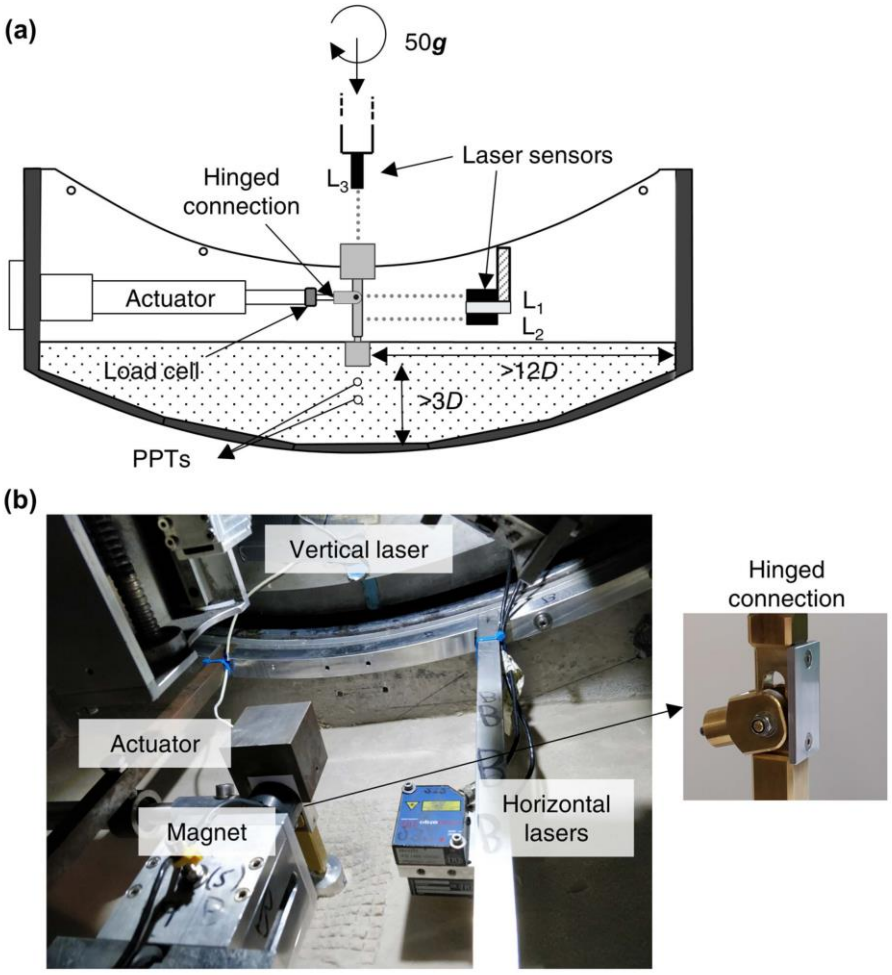

Fig.8

Accepted manuscript doi:
10.1680/jgeot.20.P.230

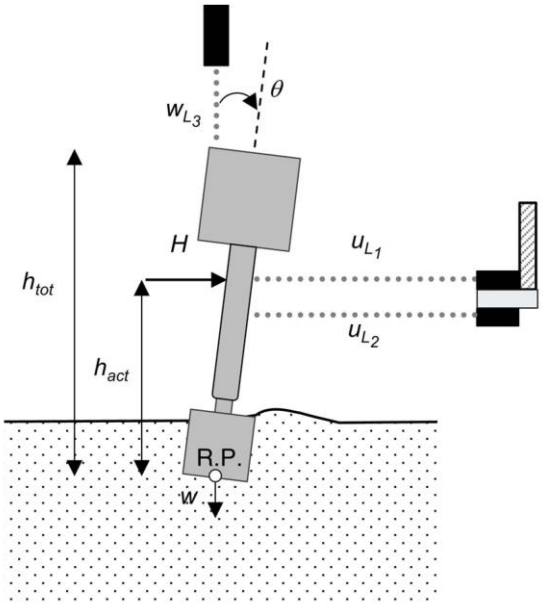

Fig.9

Accepted manuscript doi:
10.1680/jgeot.20.P.230

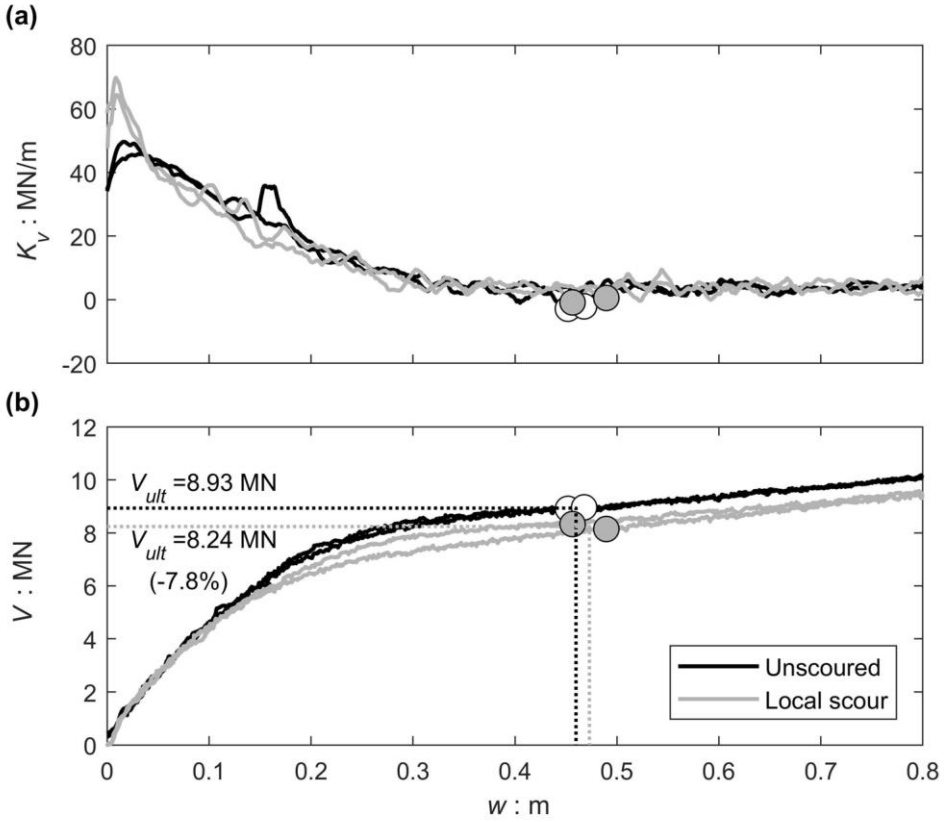

Fig.10

Accepted manuscript doi:
10.1680/jgeot.20.P.230

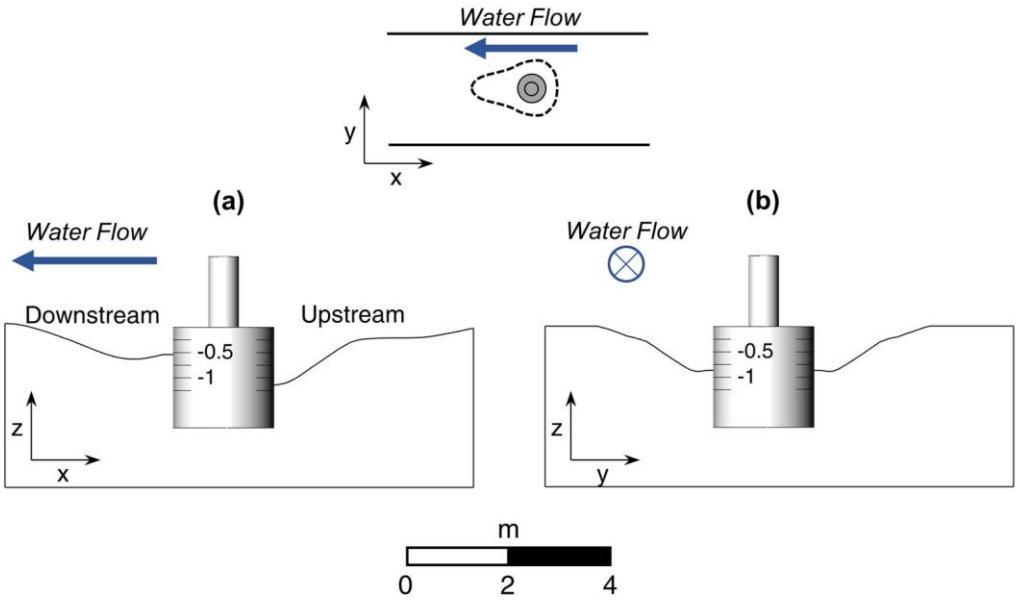

Fig.11

Accepted manuscript doi:
10.1680/jgeot.20.P.230

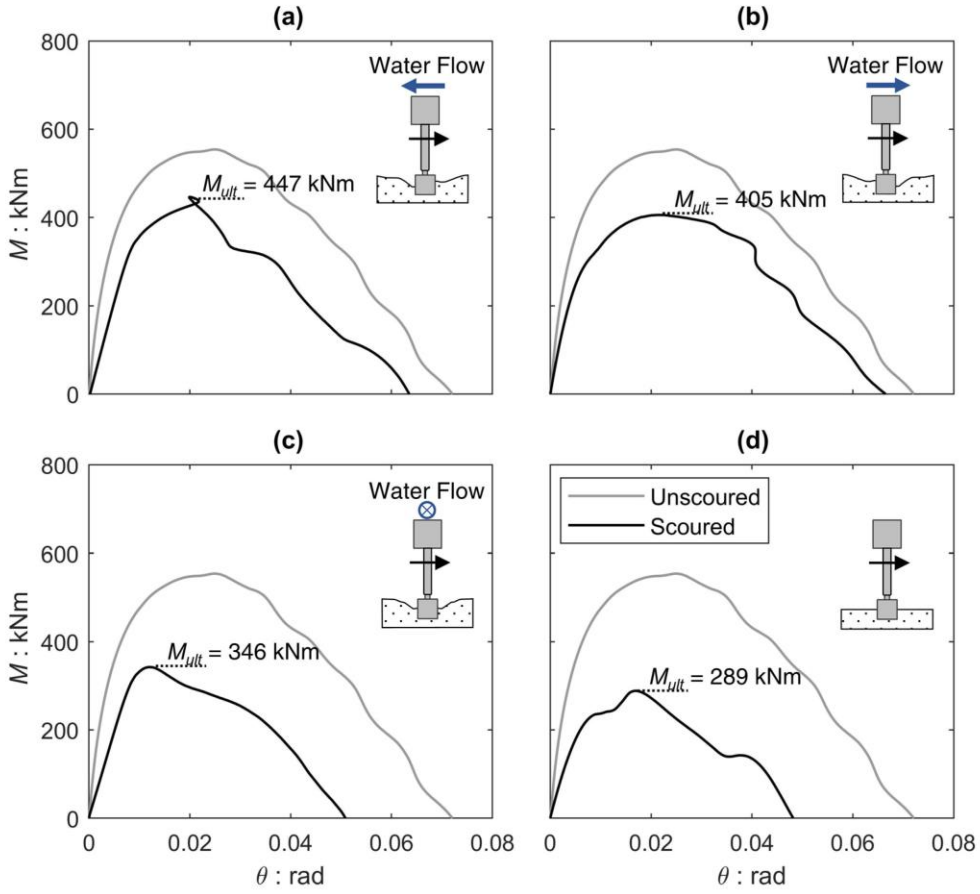

Fig.12

Accepted manuscript doi:
10.1680/jgeot.20.P.230

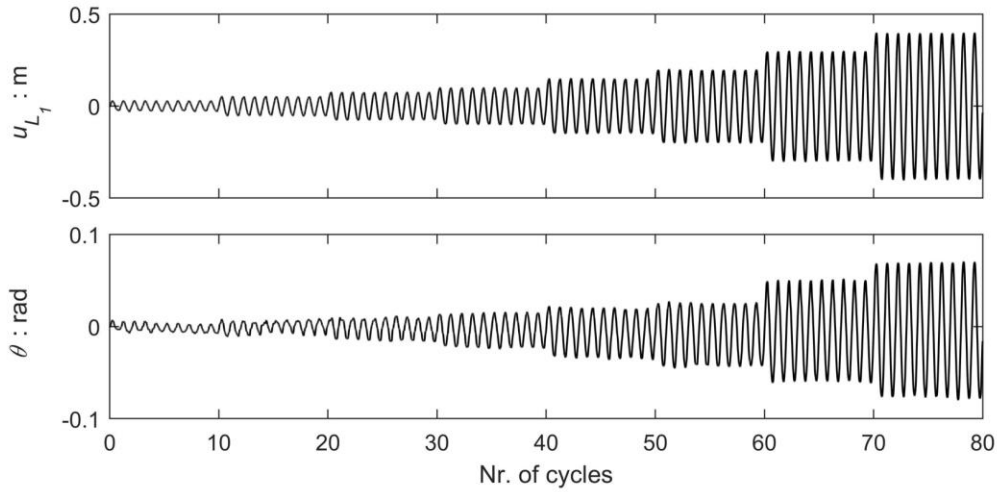

Fig.13

Accepted manuscript doi:
10.1680/jgeot.20.P.230

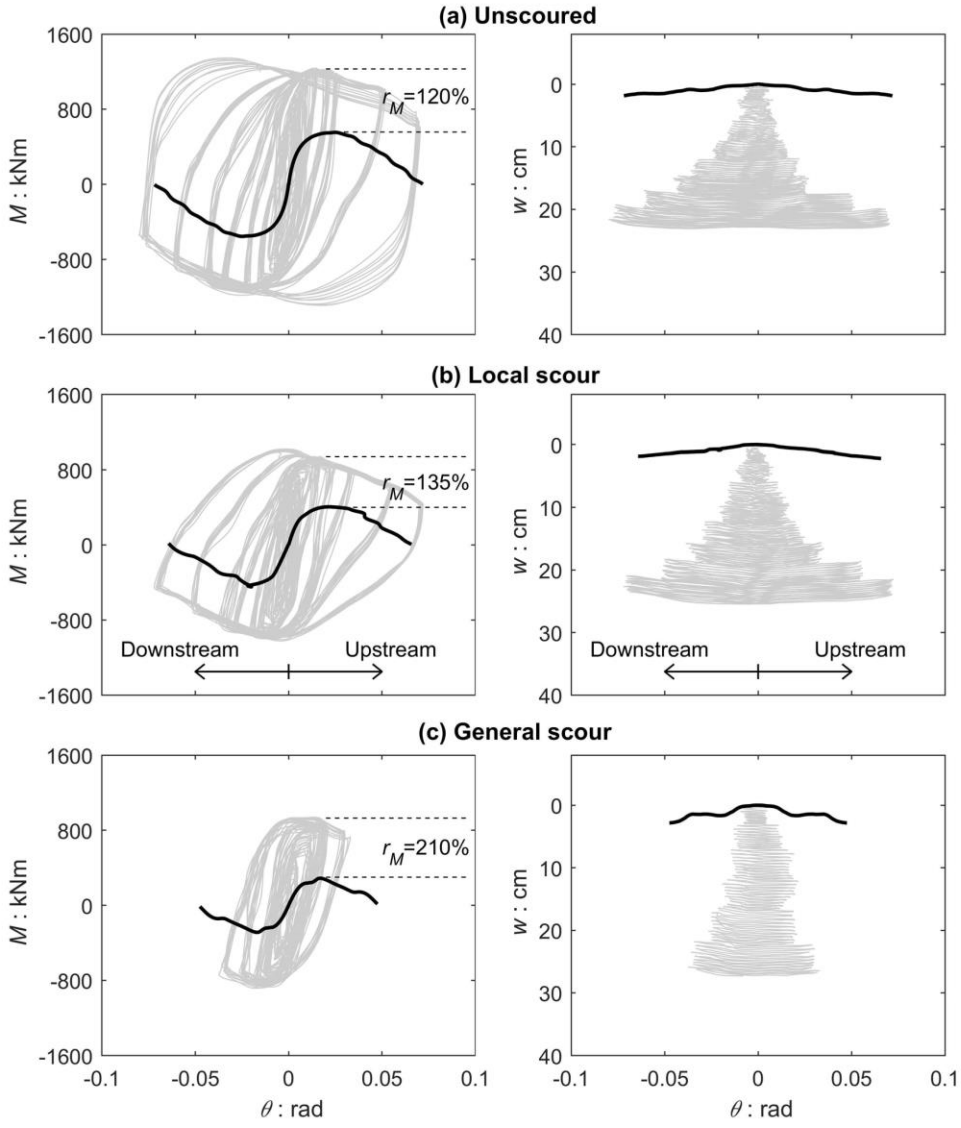

Fig.14

Accepted manuscript doi:
10.1680/jgeot.20.P.230

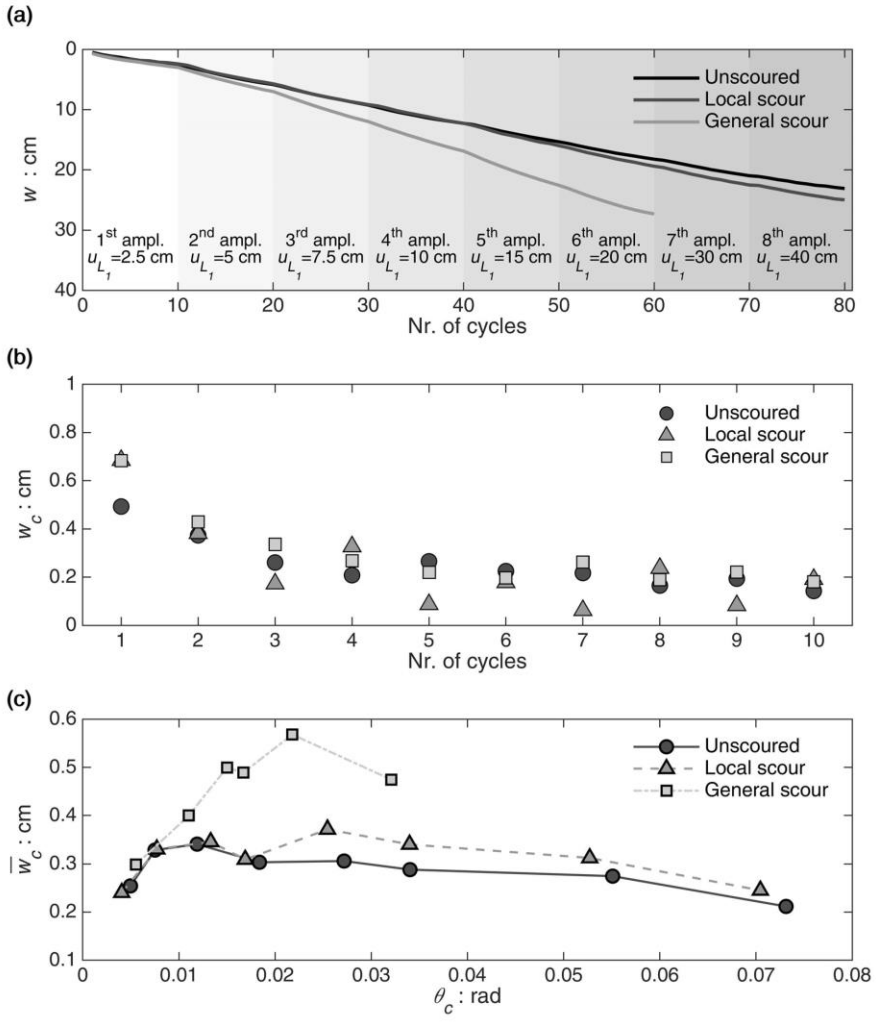

Fig.15

Accepted manuscript doi:
10.1680/jgeot.20.P.230

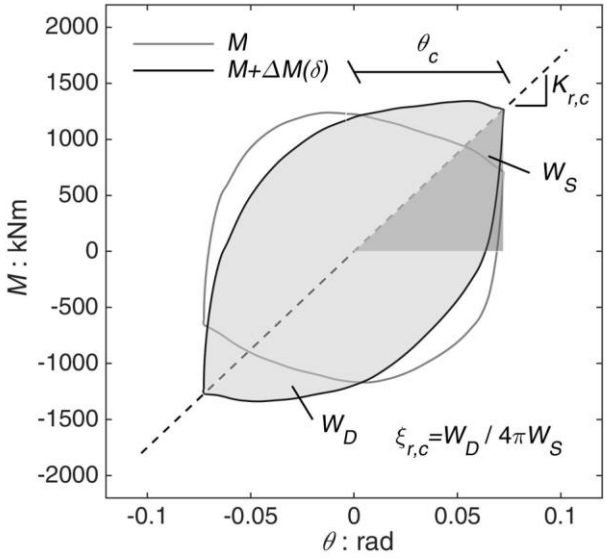

Fig.16

Accepted manuscript doi:
10.1680/jgeot.20.P.230

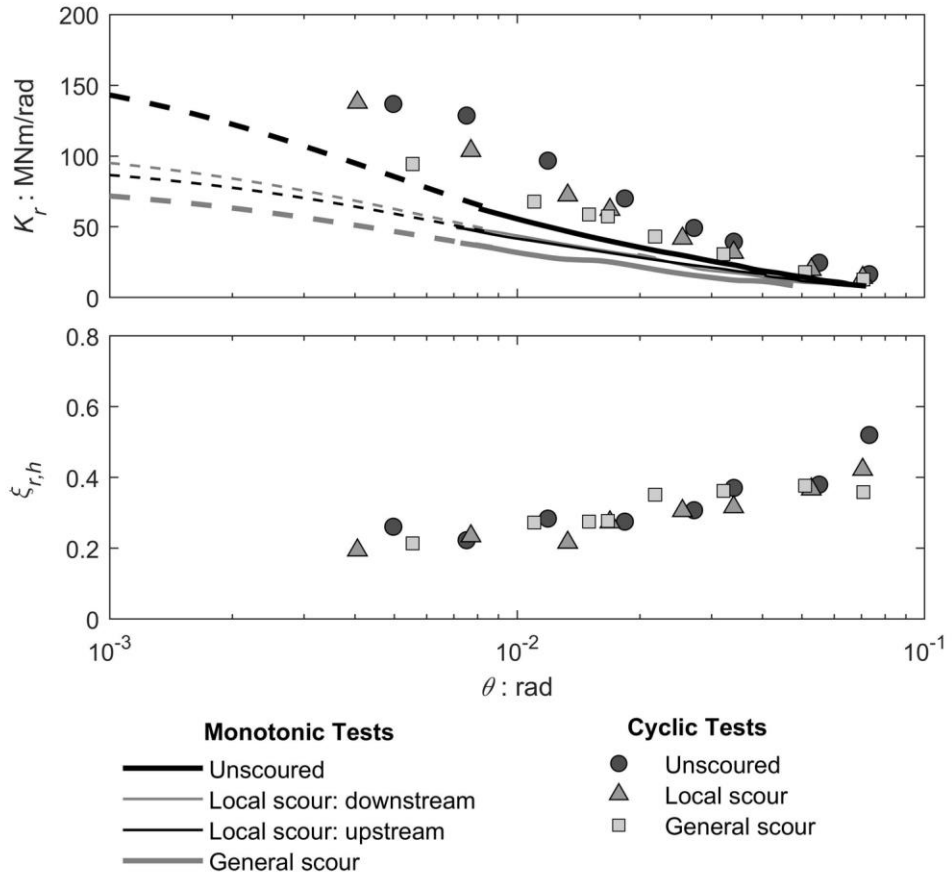

Fig.17

Accepted manuscript doi:
10.1680/jgeot.20.P.230

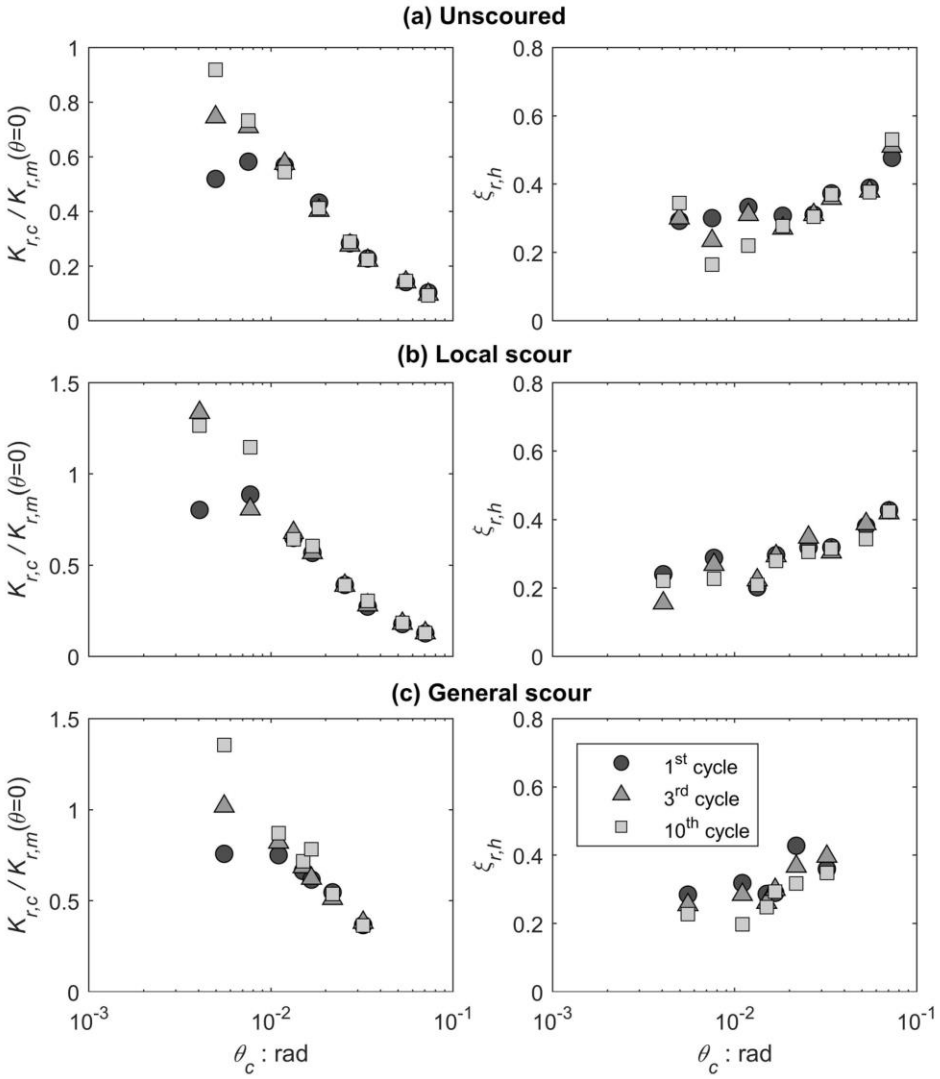

Fig.18